Title

A strategy for tissue self-organization that is robust to cellular heterogeneity and plasticity

Permalink

https://escholarship.org/uc/item/52j224hv

Author

Cerchiari, Alec Egon

Publication Date

2014

Peer reviewed|Thesis/dissertation

A strategy for tissue self-organiation that is robust to cellular heterogeneity and
plasticity

by

Alec Egon Cerchiari

DISSERTATION

Submitted in partial satisfaction of the requirements for the degree of

DOCTOR OF PHILOSOPHY

in

Bioengineering

in the

GRADUATE DIVISION

of the

UNIVERSITY OF CALIFORNIA, SAN FRANCISCO

AND

dedicated to

Ario's courage, Susanna's wisdom, and Drago's tenacity.

Acknowledgements

I would first like to thank my research mentors Dr. Zev J. Gartner and Dr. Tejal A. Desai for welcoming me to their groups, supporting me throughout my doctoral studies, and teaching me how to try to ask the right questions. I had the rare opportunity to build my research under the mentorship of two inspiring scientific leaders that have always fostered collaboration in and out of the Laboratory. Therefore, the work presented in this manuscript is the result of the efforts of a team of collaborators I cannot thank enough. Throughout the text I will use the plural voice "we" to emphasize this fact. I am referring to the vital contributions of my mentors, Dr. Mark LaBarge, Dr. James Garbe, and Dr. Matthew Thomson, to the scientific insights provided by Dr. Donna Peehl, Dr. Martha Stampfer, Dr. Mina Bissell, and Dr. Kyle Broaders, and to the critical help received by Michael Todhunter, Noel Jee, Kevin Lance, Dr. James Pinney, Dr. Justin Farlow, and Dr. Jennifer Liu. In addition, I would also like to thank all members of the Gartner and the Desai research groups for the constructive criticism provided, Dr. Lydia Sohn and Dr. Jayanta Debnath for serving on both my Qualifying Exam and Thesis committees, Dr. Tamara Alliston and Dr. Jeffrey Lotz for serving on my Qualifying Exam, Dr. Matthew Tirrell and Dr. Sanjay Kumar for introducing me to academic research, and the entire UC Berkeley – UCSF Graduate Program in Bioengineering for supporting my training financially, intellectually, and emotionally. In particular, all members of my 2010 Class Cohort have been role models, scientific partners, and close friends. Finally, I would like to thank the U.S. Department of Defense for supporting this research through the Breast Cancer Research Program Award and the National Defense Science and Engineering Graduate Fellowship.

Abstract

Classic models of cell sorting invoke differences in cell-cell cohesion to explain how multiple cell types can self-organize into spatially resolved tissues. However, tissues contain motile populations of cells that are heterogeneous in time and space and that change their cohesion in response to cell-intrinsic and extrinsic cues. The human mammary gland is a prototypical heterogeneous and dynamic tissue. Its ducts and acini comprise two concentrically arranged cell types that retain their relative spatial positions despite enormous plasticity and motility associated with development, estrous cycles, pregnancy, and the onset of malignant disease. To investigate the consequences of cellular heterogeneity and plasticity on cell positioning in this adult human tissue, we reconstituted its self-organization from aggregates of primary cells *in vitro*. We find that self-organization is dominated by a self-generated adhesive interaction between a single cell type (i.e. the basal lineage) and the tissue boundary (i.e. the Extracellular Matrix – ECM), rather than through a hierarchy of homo and heterotypic cell-cell interactions. Surprisingly, cell-ECM adhesion is binary, in that the other cell type (i.e. the luminal lineage) lacks the entire cell-ECM adhesion machinery required to adhere to the tissue-boundary. Using mathematical modeling and cell-type specific knock-down of key adhesion molecules, we show that this strategy of self-organization is robust to severe perturbations that affect cell-cell cohesion. We also find that this mechanism of self-organization is conserved in related tissues such as the human prostate. Therefore, our model supports the notion that a binary regulation of cell adhesion to the tissue boundary provides a flexible and generalizable strategy for forming and maintaining the structure of human bilayered and secretory epithelia. The model allows us to also make specific predictions about how this strategy

might breakdown in the context of injury or malignant disease. In particular, our results suggest that while decreases in cell-cell cohesion can challenge the architectural maintenance of the human mammy gland, an increase in adhesion between the luminal cell-type and the tissue-ECM boundary is the aberration that will trigger catastrophic tissue breakdown.

Table of Contents

List of Figures and Tables

Abbreviations

Cells
HMEC – human mammary epithelial cells
HPEC – human prostate epithelial cells
MEP – myoepithelial cells (NOTE: MEP are specialized basal cells but in this manuscript we use the term interchangeably with basal cells).
LEP – luminal cells

Common proteins and polymers
ECM - Extracellular Matrix
LamaV – Laminin 5
Col1 – Collagen 1
Fn1 – Fibronnectin 1
FAK – focal adhesion kinase
B1 – beta 1 integrin
A6 – alpha 6 integrin
K14 – intermediate keratin 14
K19 – intermediate keratin 19
Muc1 – mucin 1
PEG – Polyethylene Glycol
PA – Polyacrylamide

Materials and Methods
QD – quantum dots
FACS – fluorescently activated cell sorting
FC – flow cytometry
WB- western blot
IF – immunofluorescence
qPCR – quantitative polymerase chain reaction
CTG – Cell Tracker Green
CTR – Cell Tracker Red

Background
DAH – differential adhesion hypothesis
2D – two dimensional
3D – three dimensional

Units and measures
bp – base pair
g – gram
mg – miligram
μg – microgram
M – molar
mM – milimolar
μM – micromolar
nM – nanomolar
mm – milimeter
μm – micrometer
nm – nanometer
L – liter
mL – mililiter
μL- microliter
AU – Arbitrary Units

Preface

Self-assembly is a process that drives pattern formation at all scales of biological complexity. From the atomic level to society as a whole, there is always a delicate balance of forces that orchestrate structure and function. The topic of this dissertation is tissue self-assembly - a term we use interchangeably with cell sorting out, cell sorting, or tissue self-organization and that refers to the fundamental biological process that orchestrates the arrangement of cells into a patterned (or structured) tissue. *In vivo* this is a process known to heavily influence pattern formation during development, pattern maintenance during adulthood, pattern reconstitution following injury, and pattern breakdown in disease. However, understanding how cells sample their microenvironment (i.e. other cells and the ECM) in order to form multicellular complexes that become patterned functional tissues is not only of great interest to developmental, pharmaceutical, and computational biologists, it is also a topic of study for engineers that aim at reconstructing tissues using cells as building blocks and cell-instructive biomaterials as structural scaffolds.

In the field of tissue engineering there is an exquisitely wide variety of physical or chemical strategies used to pattern cells in three dimensions. However, only a handful of pioneering studies showed proper reconstitution of a functioning tissue or organ *in vitro* (see 1 for an excellent 2014 review on this topic). This is partially due to our limited understanding of the biological rules governing the self-organization of the different cellular building blocks we find in a tissue.

The Differential Adhesion Hypothesis (DAH) is a model that was largely developed by Dr. Malcolm Stainberg in the 1960s and 1970s and that offers an intuitive conceptual framework for explaining the cell sorting experiments he and others reported using dissociated embryonic cells (1, 2, 3). In the DAH, spherical scrambled patterns of cells are predicted to self-assemble into a stable conformation (Fig. 1a) based on differential homotypic and heterotypic cell-cell adhesive properties (2). In other words, given an intermediate cross-cohesion (i.e. work required to form heterotypic cell adhesion) between two different types of cells, scrambled patterns of dissociated cells will self-organize into a structure that exhibits the most cohesive type of cells in the core and the less cohesive in the periphery. Given a very high level of cross-cohesion between the two different types of cells, scrambled patterns will self-organize into scrambled architectures. On the other hand, as the cross-cohesion between the two different cell-types approaches zero, the multicellular scrambled pattern will phase separate into two different tissues regardless of the relative homotypic cohesion of the two cell-types (see Fig. 1b).

This model is oversimplifying the complexity of our cellular building blocks because it is completely neglecting signaling pathways that are triggering and are being triggered by spatial and temporal changes in and out of the cell (e.g. compaction, polarization, proliferation, gel-compliance, etc). Nevertheless, if we assume that during the first few hours following the reconstitution of dissociated cells, signaling does not alter the natural mechanical coupling of the cytoskeleton of each individual cell in the tissue (i.e. adhesion between cells), the DAH can translate into a mathematical model that explains the self-organization of many tissues reconstituted in suspension. Other models such as differential contractility, chemotaxis, or motility have also been reported and

2

experimentally validated. However, in this manuscript we use the widely cited DAH as the starting point for understanding how the presence or absence of the ECM affects cell sorting in the human mammary gland and related tissues.

In chapter 1 we summarize one of the cell-patterning technologies we have developed in order to study pattern formation of 3D cell aggregates fully embedded in different microenvironments (4). In chapter 2 we use this and other published or unpublished strategies to reconstitute the self-organization of the two different cell types found in the human mammary epithelium or the human prostate (5). As summarized in Figure 1, we show that the physicochemical properties of the ECM can dramatically alter the 3D self-organization of reconstituted cells and provide additional structural patterns that cannot be predicted using the traditional DAH framework. In chapter 3 we find that the self-organization of the human mammary gland is dominated by the adhesion of only one cell-type and the ECM rather than by differential homotypic and heterotypic cell-cell cohesive proprieties. Therefore, in order to predict the outcome of cell sorting, one must consider the relative adhesion of the different cell types to the ECM. As pictorially shown in Figure 1C, this can be visualized as the addition of the cell-ECM adhesion variable to the DAH. In chapter 4 we quantitatively explore this variable and find that in human mammary epithelia and related adult tissues, the adhesion of luminal cells to the ECM boundary is specifically maintained near zero. The advantage of using this "digital" or "binary" strategy where only one cell type (the basal type) adheres to the matrix while the other one (the luminal type) does not, offers a tremendously reliable cell sorting mechanism that is robust to cell-cell heterogeneity and plasticity. This control of tissue self-assembly by the properties of the surrounding ECM is conceptually analogous to protein folding,

where hydrophobic collapse is dominated by the energetics of hydrophobic and hydrophilic amino acid side-chain interactions with the surrounding medium.
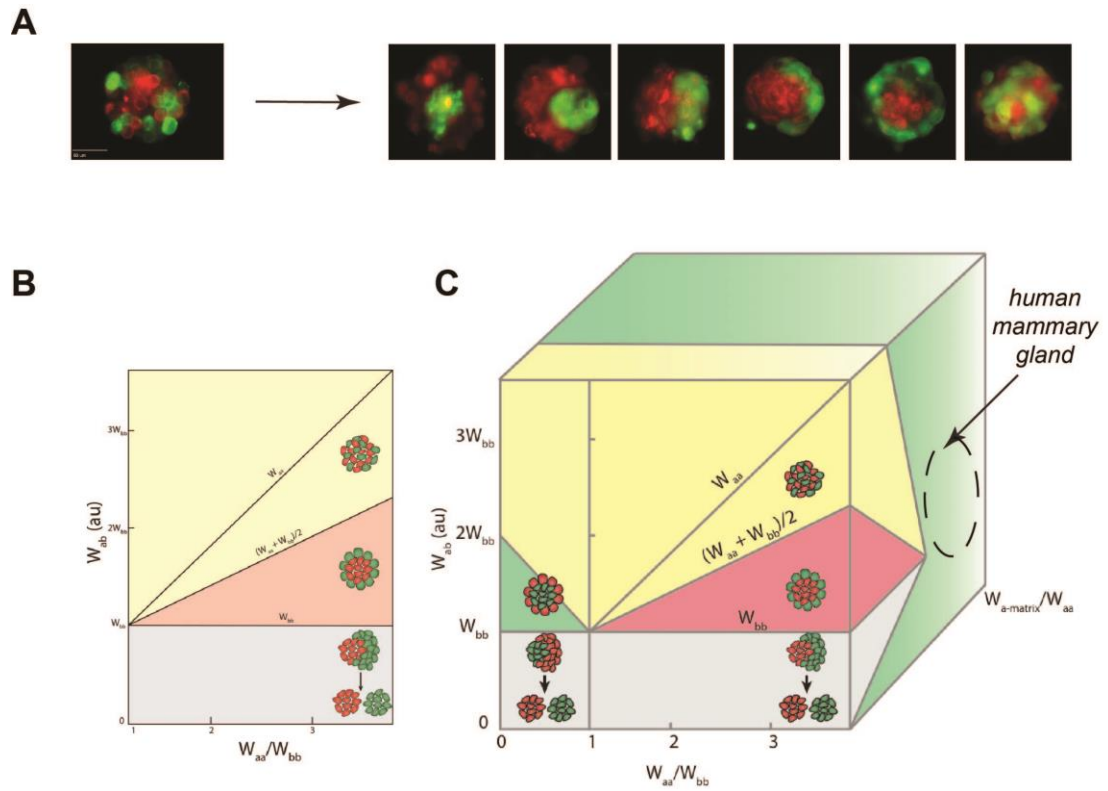
Figure 1: The Self-Organization of human mammary epithelial cells is dominated by Cell-ECM interactions. (A) Sample 40X fluorescent microscopy images of primary human mammary luminal (green) and basal (red) cells that, immediately after reconstitution (left), can self-organize into six different conformations (right). Scale bar is 50 μm **(B)** Mathematical model (adapted form 2) showing how the Differential Adhesion Hypothesis can be used to predict four of the six conformations we have experimentally observed. In this case, Waa is the work of cell-cell cohesion between red cell, Wbb is the work of cohesion between green cells, and Wab is the work of cross-cohesion between green and red cells. **(C)** Graphical visualization of how adding the work of adhesion between only one cell-type and the matrix (Wa-matrix) as a new variable in the DAH, can predict all of the conformations we have experimentally observed. The hypothesis of this thesis is that bilayered secretory epithelia such as the human mammary gland adopt a binary cell-ECM adhesion strategy for sorting heterogeneous and dynamic populations of cells.

Chapter 1

Formation of spatially and geometrically controlled 3D tissues in soft gels via Sacrificial Micromolding

1. Introduction

Three Dimensional (3D) cell culture techniques aim to mimic the *in vivo* architecture of a tissue so as to provide better models for testing drugs, studying multicellular biology, or engineering functional human tissues. A common challenge has been to develop strategies for patterning 3D multicellular structures within very soft hydrogels that best mimic the physicochemical environment of many tissues. To overcome the limitations of current methods, we use Sacrificial Micromolding to temporarily form spatially and geometrically defined 3D cell-aggregates in degradable scaffolds before transferring and culturing them in a reconstituted ECM. In this chapter we show that Sacrificial Micromolding: i) promotes cyst-formation and proper polarization of established epithelial cell lines, ii) allows quantification of the localization of lineage-specific intermediate filaments within a reconstituted mammary tissue, iii) can be used to control the lumenization-state of renal epithelial cysts as a function of tissue size, and iv) can be used to localize foreign objects such as drug-carriers or nanoparticles within the luminal compartment of a reconstituted intestinal cysts. Finally, we introduce the use of this cell-patterning technology for studying the self-organization of human glandular epithelial tissues in vitro.

2. Background

In addition to biochemical signals, the mechanical environment of a tissue can exert a profound influence on cell phenotype. Consequently, 3D tissue culture models have become the gold standard for assays that aim to recapitulate the *in vivo* phenotype of cells and tissues in a dish (6, 7). In these models, primary or cultured cells are typically seeded on top or within hydrogels that support the growth, differentiation, and/or maintenance of the cells in 3D. However, these approaches do not provide any geometric constraints and the tissues that grow tend to be heterogeneous in their size, shape, and position within the gel. One popular approach for controlling tissue geometry in 3D culture is the use of photolithographic techniques for patterning or replica-molding scaffolds that can accommodate collections of cells at high density and with a well-defined geometry (8). The materials typically used in this approach are those that can be readily patterned by photolithography (e.g. epoxy-based photoresists, UV-reactive polymers, etc.) or micromolded by soft-lithorgaphy (e.g. elastomers, agaorse, etc). For example, PDMS, Agarose, or Poly (ethylene glycol) microwells have been used extensively as semi-3D (or 2.5D) cell-culture platforms that produce complex tissue geometries at low cost and high-throughput (9-11). However, although these materials are easy to work with, they do not mimic the physicochemical complexity of the *in vivo* ECM. Moreover, these substrates are generally limited to 3D extrusions of 2D patterns and do not fully encapsulate the reconstituted tissue. Therefore, photolithographic approaches have been adapted in order to form spatially and geometrically defined 3D patterns within biomimetic ECM gels. For example, Nelson *et. al.* utilized an elastomeric array of well-defined posts to imprint

microcavities within type I collagen gels (12). When seeded with cells and overlaid with additional collagen, this method offered an unprecedented level of control over the geometry and spatial organization of reconstituted microtissues. Nevertheless, this strategy is challenging to implement when dealing with very soft gels such as the popular, laminin-rich, reconstituted basement membrane hydrogel known as Matrigel. Matrigel is unparalleled in its emulation of the basement membrane *in vivo*, due to a multi-factorial composition of distinct matrix components (laminin, collagen IV, entactin, etc.) as well as its mechanical properties that are well matched to many soft tissues *in vivo* (13, 14). Unlike other ECM models, Matrigel forms stable but extremely soft gels (< 0.5 kPa) (15), that promote morphogenesis and improve the diffusion of biochemical factors throughout the 3D matrix. However, the same "liquid-like" time-dependent viscoelastic properties that define the gel's low stiffness also challenge the reliable geometric patterning of this soft material. To date, some techniques for patterning Matrigel do exist (16). Nevertheless, these are not amenable to forming spatially and geometrically controlled multicellular aggregates. Inspired by previous reports that validated the use of degradable materials such as gelatin for patterning microfluidic channels embedded in Collagen or Fibrin (17, 18), we envisioned using this material in order to temporarily mold cell-aggregates in 3D. Here, we identify conditions that preserve geometry and localization of individual tissues after gentle degradation of the sacrificial mold and transfer to soft gels. This approach allows us to predetermine the initial size, geometry, and location of cell-aggregates fully embedded in Matrigel.

3. Materials and Methods

3.1. Cell lines in two dimensional culture conditions

MCF10A, MDCK, Caco 2, and 4th passage primary human mammary epithelial cells (HMEC) derived from the reduction mammoplasty of human specimen 240L were maintained in 2D tissue cultures as previously described (9, 19, 20).

3.2. Fabrication of sacrificial microwells

Using the Biomedical Micro- and Nano-Fabrication Center (BMNC) at UCSF, freestanding SU-8 features on silicon wafers were fabricated using photolithographic techniques. All recipes used for photopatterning were adapted from MicroChem's technical specification sheets. For instance, to obtain circular microwells 120 μm in diameter and 80 μm deep, SU-8 2035 (MicroChem) was spun on the substrate at a speed of 500 rpm for 10 seconds followed by a 1250 rpm spin for 30 seconds. The wafer was then soft-baked for 5 minutes at 65 ˚C and for 10 minutes at 95 ˚C, UV-exposed in contact mode with an exposure energy of 215 mJ/cm^2 (through a photo-mask designed in AutoCAD and printed by Outputcity Co.), post-exposure baked for 5 minutes at 65 ˚C and for 10 minutes at 95 ˚C, and developed in SU-8 developer (MicroChem) for at least 20 minutes. The patterned substrate was finally washed with isopropanol/water and hard baked at 150 ˚C for 1 hour prior to measuring pillar heights using a stylus-profilometer (Ambios XP2) and visualizing the quality of the patterned wafer by SEM (NovelX

mySEM). The silicon master was used to create PDMS micropillars by pouring a Sylgard 184 silicone elastomer kit (Dow Corning) onto the patterned wafer using a base:crosslinker ratio of 10:1. After overnight incubation at 65 ˚C, the cured PDMS template was finally peeled off the substrate and incubated with Sigmacote (Sl-2, Sigma-Aldrich) for a few hours before micromolding sacrificial microwells made of 8% (w/v) gelatin (Knox Gelatine) in phosphate buffered saline (PBS). To ease the release of PDMS from the protein-based sacrificial layer, other passivation strategies could also be used (12, 21).

3.3. Sacrificial Micromolding

Before each experiment, cells were dissociated, resuspended at a concentration of 10^6/mL, and centrifuged into the wells at 160 x g at 4 ˚C for 4 minutes immediately after PDMS removal. Excess cells were then washed away with medium. To transfer the remaining physically confined cell-aggregates from gelatin to Matrigel, we carefully peeled the thin gelatin mold with cell-clusters from the substrate, inverted it over a Matrigel slab (previously set for 30 minutes at 37 °C), incubated the dish at 37 °C for 1 hour, gently washed away the melted gelatin with media, and finally overlaid more Matrigel on top before adding media for long-term culture. When forming heterotypic tissues using live-cell staining, 4th passage HMEC were FACS-purified into myoepithelial (MEP) and luminal (LEP) lineages using established cell-surface markers (CD10 for MEP and CD227 for LEP) as detailed in chapter 2 and stained with cytosolic dyes before being loaded into the sacrificial gelatin template. The live staining procedure was carried out following the manufacturer's procedure and required resuspending sorted LEP or MEP in 10 mL of PBS,

incubating with 1 μL of either 10 μM Cell Tracker Green (Invitrogen) for LEP or 10 μM Cell Tracker Red (Invitrogen) for MEP for 5 minutes at 37 ˚C, pelleting, discarding supernatant, and resuspending at the desired concentration (i.e. 10^6/mL). Before loading the sacrificial microwells, stained LEP and MEP were mixed at a 1:1 ratio. Figures 1A and 1B offer a schematic summary of the Sacrificial Micromolding method and representative images of MDCK cell-clusters transferred from a gelatin sacrificial mold to a Matrigel matrix.

3.4. Characterization of hydrogels

The viscosities of Matrigel, fibrin and gelatin were measured as a function of temperature and/or time. Matrigel (Lot 07898) was purchased from BD Biosciences (354230) and was used undiluted. Fibrin gels were made by mixing a solution of 5 mg/mL fibrinogen (Sigma F8630) and 0.1 units/mL thrombin (Sigma T7513) in PBS. Gelatin (Knox ORIGINAL Gelatine) was purchased at Safeway and diluted to 8% w/v in boiling PBS. All viscosity measurements were accomplished using a BlackPearl Viscometer (ATS Rheosystems) and a 30 mm parallel plate (with 1 mm gap) insert (ATS Rheosystems). For the thermal sweeps of Matrigel and gelatin (Fig. 1C top) we measured gel viscosity as a function of increasing (for Matrigel) or decreasing (for gelatin) temperature. For the time sweeps of fibrin and gelatin (Fig. 1C bottom) we measured viscosity as a function of time at constant 37 °C. All parameters used for captured measurements were controlled using Rheosys Micra software (ATS Rheosystems).

3.5. Immunofluorescence

All microtissues were fixed with 4% Formaldehyde (in PBS) for 20 minutes and then incubated in blocking buffer (10% heat inactivated goat serum in PBS + 0.5% triton X-100) at 4 ˚C for at least 1 day. Primary antibodies were then diluted in blocking buffer and added to the sample as summarized in Table 1. After at least one day incubating at 4 ˚C with the primary antibody, all microtissues were washed several times with PBS + 0.05% Triton-X for at least one day and incubated with Alexafluor-conjugated secondary antibodies (Life Technologies) diluted at a concentration of 1:200 in blocking buffer for approximately 1 day. Before imaging the clusters, all samples were washed with PBS + 0.05% Triton-X + 1 μg/mL DAPI for at least 1 day.

Antibody	Product	Application
Anti-human CD324 (E-Cadherin)	BioLegend 324112	IF (1:100)
Anti-human CD49f (Alpha 6 Integrin)	Millipore MAB1378	IF (1:50)
Anti-dog GP135 (custom made)	Mostov Lab (UCSF)	IF (1:100)
Anti-human beta-catenin	Santa Cruz 7199	IF (1:100)
Alexa Fluor 488 Phalloidin	Life Tech A12379	IF (1:200)
Anti-human CD227-FITC (Muc1-FITC)	BD 559774	FACS (1:50)
Anti-human CD10-APC (Calla-APC)	Biolegend 312210	FACS (1:200)

Table 1. List of antibodies used, product numbers, and application (IF: immunofluorescence; FACS: fluorescently activated cell sorting). The dilution used for each application is reported in parentheses.

3.6. Image acquisition

All confocal microscopy images were acquired using an inverted confocal microscope (Zeiss Cell Observer Z1) equipped with a Yokagawa spinning disk, an Evolve EM-CCD camera (Photometrics), and running Zeiss Zen Software. All other images were acquired using an inverted epifluoresent microscope (Zeiss Axiovert 200M) running SlideBook software.

3.7. Quantification

For quantifying the localization of lineage-specific keratin markers within the reconstituted HMEC microtissue, we collected 20 confocal (40X magnification) images of 20 fixed and stained structures, cropped the images to the exact size of the spherical tissue, binarized the fluorescent signal from the green (for Keratin 19) and red (for Keratin 14) channels, stacked/resized to the smallest sample of all images collected, and plotted the normalized average radial reslice of the normalized average (K14 and K19) signals. Image analysis was conducted using FIJI software. For quantifying the number of lumens formed as a function of the diameter of the reconstituted microtissue, we first measured the diameter of 30 microtissues in FIJI and plotted the average and standard deviation of our measurements against the known diameter of the PDMS post (Fig. 4C). We then visually counted the number of lumens formed as determined by Z-stack confocal analysis of 11 MDCK tissues (for each size) fixed and stained with phalloidin and DAPI and plotted the average of the number of lumens as a function of the average diameter of the tissue (Fig.

4D). Lumens were defined as phalloidin-stained actin rings surrounded by DAPI-stained

nuclei.
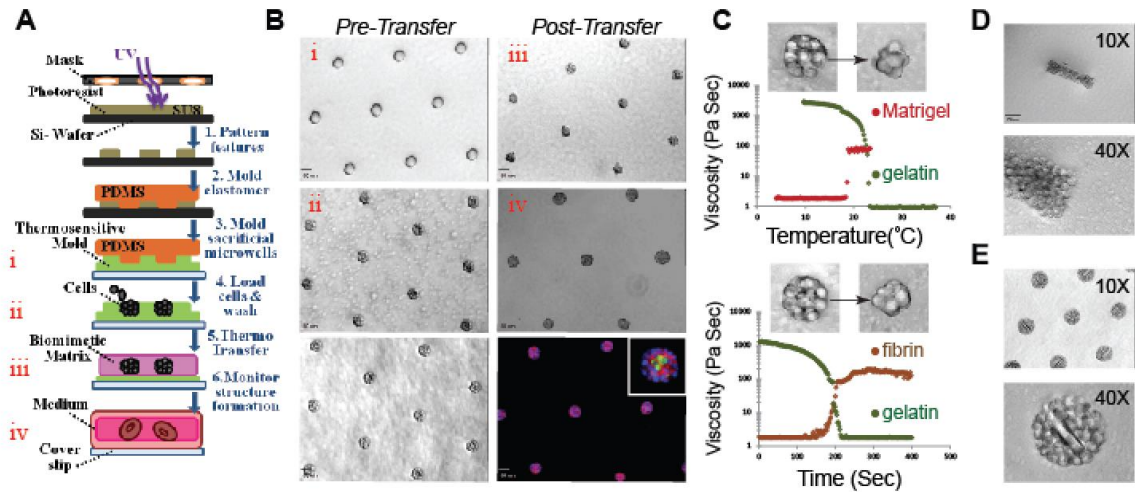
Figure 1: Sacrificial Micromolding of 3D tissues in soft gels. **(A)** Schematic representation of the formation and use of sacrificial gelatin micromolds for patterning 3D microtissues in soft gels. **(B)** 10X microscopy images of empty gelatin microwells (i), gelatin microwells loaded with MDCK cells (ii), gelatin microwells loaded with MDCK cells and washed with media to remove excess cells (bottom left), MDCK cell-clusters transferred to Matrigel (iii), MDCK cysts in Matrigel after 4 days in culture (iv), and MDCK cysts fixed and stained for β-catenin (red), nuclei (blue), and GP130 (green) (bottom right). The insert is a representative microtissue at 40X magnification. Scale bars are 50 μm. **(C)** Plots of the viscosity of gelatin and Matrigel as a function of temperature (top) and of the viscosity of gelatin and fibrin (following the addition of thrombin) as a function of time (at 37 °C. bottom). The inset images are 40X phase contrast microscopy images of representative clusters transferred from gelatin to the indicated soft gel. **(D)** 10X (top) and 40X (bottom) phase contrast microscopy images of a cell-aggregate molded with a rectangular geometry and transfered to Matrigel. Scale bar is 100 μm. **(E)** 10X (top) and 40X (bottom) phase contrast microscopy images of spherical cell-aggregate clusters molded and transferred to Matrigel with PEG-microrods. Scale bar are 100 μm.

4. Results

4.1. Phase-transitions of gelatin and Sacrificial Micromolding

Gelatin is a food product with a phase-transition that occurs close to body temperature (Fig. 1C). When dissolved in boiling PBS, the gelatin powder forms a liquid that gelates upon refrigeration. As shown in Figure 1C, when a 1 mm slab of cooled gelatin is incubated at 37 °C, its viscosity drops dramatically. On the other hand, the viscosity of a liquid drop of Matrigel sharply increases as the gel is brought towards the same physiological temperature. Given the relative proximity of the phase transition temperatures of these two protein-based hydrogels, we explored the use of gelatin as a moldable sacrificial layer to form defined patterns of cell aggregates in 3D at 4 °C; and Matrigel as a material for collecting and culturing the molded cell aggregates in 3D at 37 °C (Fig. 1B). Since Sacrificial Micromolding can be used to encapsulate microtissues in other gels with similar controlled liquid-gel transitions like fibrin (Fig. 1C, bottom), this technique provides a versatile mean for culturing spatially resolved multicellular 3D tissues in soft gels. As shown in Figure 1D, Sacrificial Micromolding is not limited to the 3D culture of spherical microtissues and the initial geometry of the reconstituted cell-aggregates can be easily varied by simply changing the geometric dimensions of the PDMS stamps used to imprint the sacrificial microcavities. Unlike other chemical or mechanical strategies used to pattern cells, the physical confinement used to define the initial shape of the cell-aggregate in gelatin can be readily used to also accommodate drug-carriers,

scaffolds, or foreign objects like PEG-microrods (Fig. 1E). Overall, this technique offers a versatile platform for patterning spatially and geometrically defined tissues in soft gels.

4.2. Patterning MDCK, MCF10A, and Caco2 Cysts by Sacrificial Micromolding

To validate the use of Sacrificial Micromolding for 3D tissue culture, we investigated whether epithelial cell-lines known to form hollow cysts when cultured in Matrigel could recapitulate their established polarized tissue architecture when transferred from gelatin microwells to Matrigel (22-25). We found that after only 4 days, all cell-lines established polarity and features indicative of cyst-formation (Fig. 2). GP135 and actin were found lining the lumen of MDCK and Caco2 microtissues, respectively (Fig 1B bottom right insert and Fig. 2B bottom right). Consistent with previous reports, MCF10A cells did not establish true apical-basal polarity *in vitro* as do MDCK and Caco2 (Fig. 2B top right) (22). However, MCF10A microtissues did establish tissue-level polarity, properly localizing α_6 Integrin to the basal surface and E-cadherin to cell-cell junctions.
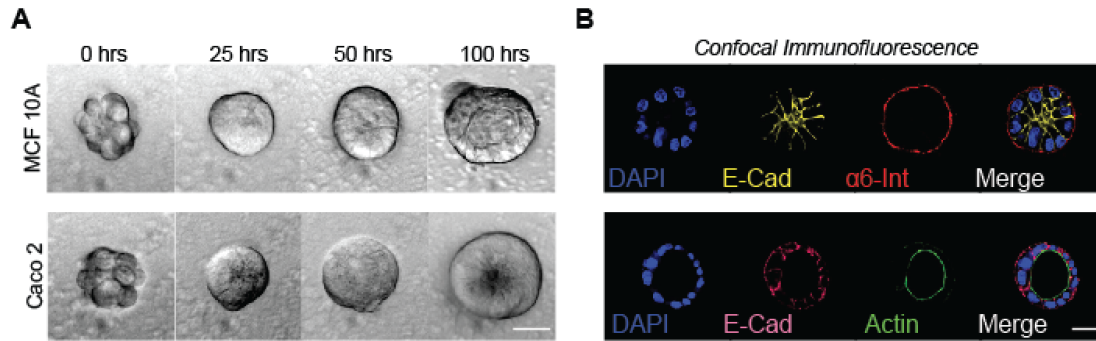
Figure 2: Polarization and lumen formation of epithelial cell lines. (A) 40X phase contrast microscopy images of MCF10A (top) and Caco2 (bottom) cell-clusters at different time points. The lumen edge is visible as a ring of contrast in the MCF10A phase contrast image. **(B)** 40X confocal microscopy images of MCF10A (top) and Caco2 (bottom) microtissues fixed and stained for the localization of polarity markers (α_6 integrin for MC10A, Actin for Caco2). The lumen edge is visible as an actin ring in the Caco2 image. Scale bars are 20 μm.

4.3. Formation of properly structured heterotypic mammary epithelial tissues by Sacrificial Micromolding

Cell-patterning can define the initial spatial position of cells in a gel, but shortly after tissue reconstitution, cells can self-organize according to the delicate balance of intrinsic cues they are experiencing (9). We therefore tested whether Sacrificial Micromolding would support the proper self-organization of the two cell types found in the human mammary epithelium. Encouragingly, we found that heterogeneous mixtures of luminal and myoepithelial cells self-organized and maintained architecture after 2 days in Matrigel (Fig. 3C). We quantified the extent of organization in these tissues utilizing immunofluorescence to characterize the average spatial localization of lineage specific

19

keratin markers at 1 hour (Fig. 3D) and 48 hours (Fig. 3E). Consistent with the *in vivo* tissue organization, we reproducibly found luminal (LEP: K14-/K19+) epithelial cells in the core surrounded by an outer layer of myoepithelial (MEP: K14+/K19-) cells. Therefore, Sacrificial Micromolding and transfer to Matrigel provide an efficient means of forming and culturing primary human MEP and LEP into tissues that mimic the *in vivo* architecture. In contrast, formation of identical cell aggregates in PDMS microwells was not a suitable method for long-term culture. In PDMS microwells we found that MEP begin to spread over the stiff and adhesive two dimensional interface and the compacted architecture is lost when cell-aggregates interact with the elastomer for more than 24 hours (Fig. 3B).
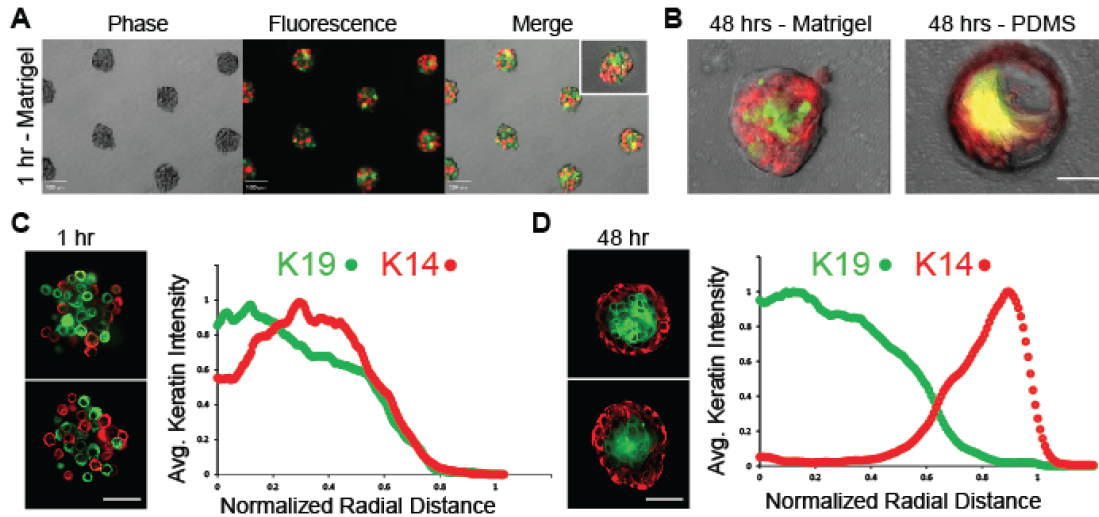
Figure 3: Self-Organization of human mammary epithelial cells (HMEC) in Matrigel. (A) 10X phase and fluorescent microscopy images of heterogeneous mixtures of luminal (green) and myoepithelial cells (red) transferred to Matrigel by Sacrificial Micromolding. Scale bars are 100 μm. **(B)** 40X overlays of phase contrast and fluorescence microscopy images of live heterogeneous mixtures of luminal (stained with Cell Tracker Green) and myoepithelial cells (stained with Cell Tracker Red) in Matrigel (left) and PDMS (right) 48 hours after transfer. Scale bar is 50 μm. **(C)** 40X confocal microscopy images of reconstituted HMEC cell-aggregates fixed and stained for lineage-specific keratin markers (K19 for luminal cells in green, K14 for myoepithelial cells in red) 1 hour after transfer to Matrigel (left). Average keratin intensity as a function of normalized radial distance from the center of spherical aggregates is plotted to the right of the images (N = 20). **(D)** Representative tissues and average keratin intensity plots after 48 hours of culture in Matrigel (N = 20). Scale bar is 50 μm.

4.4. Lumenization as a function of tissue size

One of the advantages of using Sacrificial Micromolding for 3D tissue formation and culture is the precise control over the initial size and spacing of reconstituted cell-aggregates. To demonstrate such control, we reconstituted MDCK cell-aggregates of different sizes from single cells and cultured them for 4 days in Matrigel. Sacrificial Micromolding reproducibly defined the average number of cells within each cell-aggregate (Fig. 4). Therefore, we used this feature of the technique to quantify the average number of lumens formed as a function of microtissue diameter at a fixed time point after aggregation (Fig. 4C). Previous studies indicate that lumen formation in MDCK occurs spontaneously at the interface between groups of cells touching the extracellular matrix (25). When multiple lumen form in a tissue, they can coalesce into a single structure as morphogenesis progresses. However, the precise relationship between tissue size and lumen formation has not been established. At 4 days, we noticed a logarithmic relationship between the number of lumens in each tissue and the number of cells used to form the initial aggregate (Fig. 4C). In other words, we estimate that after 4 days, there is one lumen every 22-30 cells regardless of tissue size. Interestingly, many of these lumen formed between aggregates of cells not in contact with the surrounding Matrigel. Future studies of multicellular cyst formation as a function of time and geometry will help to elucidate how these multicellular constructs regulate lumen formation and coalescence.
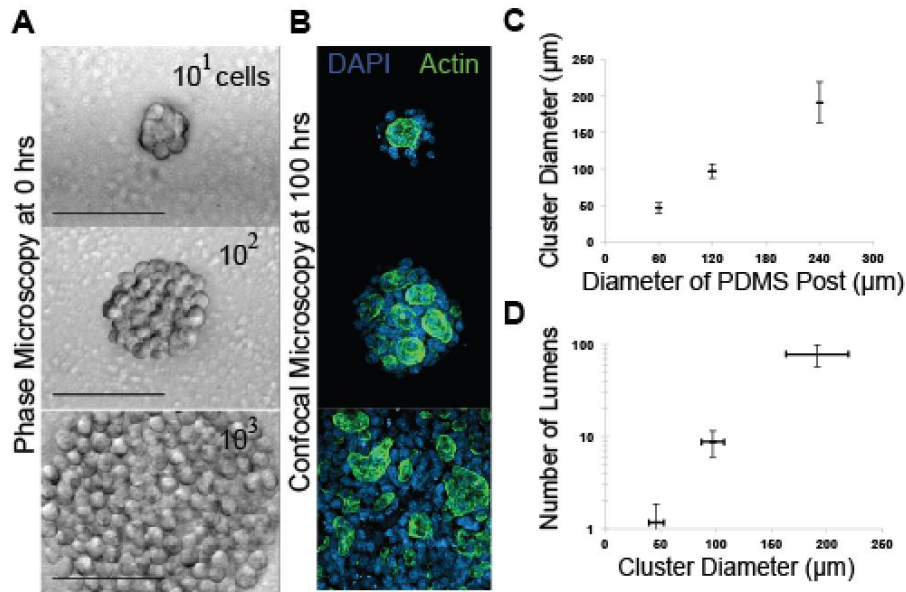
Figure 4: Quantifying the extent of lumen formation as a function of aggregate size. (A) 40X phase contrast microscopy images of MDCK cell-aggregates transferred to Matrigel via Sacrificial Micromodling 1 hour after transfer. Scale bars are 100 µm. **(B)** 40X confocal microscopy images of MDCK microtissues fixed and stained with DAPI (blue) and Phalloidin (green) after 4 days of culture. **(C)** Quantification of cluster diameter (N=30) as a function of the diameter of the PDMS posts used to imprint the sacrificial gelatin microwells (all PDMS posts had a height of 80 µm). **(D)** Quantification of the number of lumens formed as a function of cluster-diameter (N=11).

4.5. Non-intrusive localization of micron-sized carriers within the lumen of 3D Cysts

Another advantage of of using Sacrificial Micromolding for patterning cells in 3D biomimetic gels is the extreme ease with which we can incorporate foreign objects such as PEG microrods (Fig. 1E), FITC-BSA loaded PEG-microcubes, or QD-605 loaded Dextrin-microspheres (Fig. 5A, top) within the reconstituted tissue. Interestingly, we noticed that when these minimally adhesive carriers were surrounded by Cyst forming epithelial cells such as Caco2 (Fig. 5A, bottom) the object did not prevent morphogenesis and, after 1 week in culture, could be fully incorporated within the apical compartment of the lumenized cyst (Fig. 5B). Microparticles such as these have been well-studied as vehicles for drug delivery or chemical sensors, but these types of devices have never before had such intimate access to the internal lumen of a reconstituted 3D tissue. Therefore, we expect that this exciting result will enable us to study drug release through epithelial barriers in 3D *in vitro* systems with a level of biomimicry that is unachievable by current popular techniques such as the 2D dual-chamber Transwell systems.
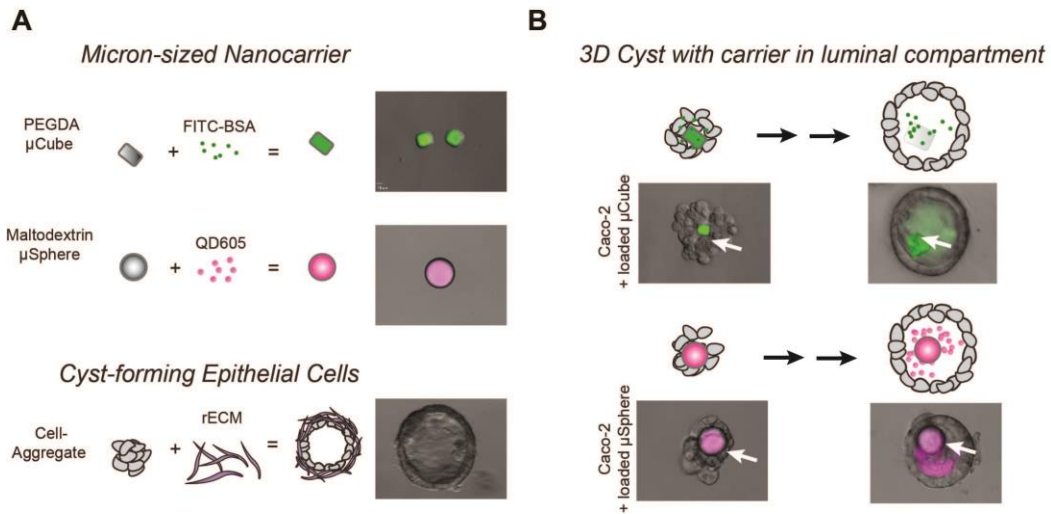
Figure 5: Non-intrusive localization of micron-sized carriers within the lumen of 3D Cysts. (A) Schematic representation and fluorescent microscopy image of sample micron-sized carriers made out of PEG or MaltoDextrin and of Caco2 cyst formation after 6 days in Matrigel. (**B**) Schematic representation and 40x fluorescent microscopy images of Lumen formation around the embedded carrier (white arrows) after 1 hour (left) and 1 week in culture (right). Scale bar is 10 μm.

5. Discussion

Tissues demonstrate a high degree of architectural complexity *in vivo*. The capacity to effectively and stably reproduce these structures *in vitro* is critical for the study and engineering of tissue-level processes in 3D. We take advantage of the phase-transition properties of gelatin (Fig. 1C) to precisely define the initial size, geometry, and location of reconstituted tissues fully embedded in very soft gels like Matrigel and fibrin. We find that when spherical structures of approximately ten MDCK, MCF10A, or Caco2 cells were cultured in Matrigel, the reconstituted cell-aggregates formed properly polarized

microtissues containing a single lumen after only four days (Fig. 2) – a process that may take longer when starting from single cells embedded in Matrigel. For the first time, we were also able to use a cell-patterning technology in order to non-intrusively accommodate microcarriers within the lumen of 3D cysts (Fig. 5) and to carefully tune the dimensions of epithelial cell-aggregates in order to control the number of lumens formed within the tissue (Fig. 3). Further manipulation of gel formulation will be required to identify the optimal physicochemical properties necessary to promote distinct aspects of morphogenesis characteristic of each tissue type. For example, addition of low concentrations of collagen or increasing gel stiffness with synthetic materials could promote cell dissemination or branching morphogenesis (26, 27).

Overall, Sacrificial Micromolding is a cell-patterning technology that allows us to predetermine the initial location, geometry, and size of a community of cells fully embedded into a biomimetic hydrogel. However cells are dynamic living building blocks that exhibit active biological processes such as differential motility and contractility. Therefore, immediately after patterning, cells will start "sampling" their micro-environment (i.e. other cells and the ECM) and rearranging into the most "stable" biological architecture. This process is known as cell-sorting out, tissue self-assembly, or self-organization and is the topic of study in the subsequent chapters.

Chapter 2

Cell-Cell vs. Cell-ECM adhesion: Self-Organization of human glandular tissues in the presence and absence of a reconstituted basement membrane.

1. Introduction

Tissues contain dynamic populations of cells that are heterogeneous in time and space. It is unclear how heterogeneous populations of cells can coordinate their self-organization into spatially ordered tissues. The human mammary gland is a prototypical heterogeneous and dynamic tissue. Its ducts and acini comprise a bilayered epithelium that retains the relative spatial position of luminal and basal cells despite enormous plasticity associate with natural biological processes like development, pregnancy, lactation, or gland involution.

To investigate the consequences of cellular heterogeneity and plasticity on cell positioning in the mammary gland, we reconstituted its self-organization from aggregates of primary cells *in vitro*. In this chapter we discuss previous art and the cell sorting or self-organization experiments we have developed for reconstituting luminal and basal cells directly after isolating them from uncultured human tissue or cultured primary human epithelial cells via Fluorescently Activated Cell Sorting (FACS). To reassemble the dissociated cells in 3D and in different microenvironments, we use chemical or mechanical cell-patterning strategies like Sacrificial Micromolding. Our material of choice for simulating a non-adhesive microenvironment that does not provide a substrate for cell-ECM interactions is agarose. Our material of choice for mimicking the adhesive

microenvironment of human glandular epithelia is the laminin-rich reconstituted basement membrane gel known as Matrigel.

2. Background

Self-organization is a process that contributes to pattern formation and repair at all scales of biological complexity. At the tissue scale, defining robust strategies of cellular self-organization is critical for engineering tissues, as well as for understanding development and the onset of diseases such as cancer (28). During development, two or more populations of motile cells can self-organize into structurally ordered tissues by a process referred to as cell-sorting (2, 3, 29, 30). The final position of the cells corresponds to a configuration that maximizes the formation of the most cohesive cellular interfaces (2). For example, with an intermediate level of cross cohesion, the most self-cohesive cell type is typically found in the tissue core, with the less cohesive cell type spread around the tissue surface.

In order for self-organization to proceed robustly by this differential adhesion strategy, a tissue requires a clearly delineated hierarchy of homo and heterotypic cell-cell cohesive interactions. During adulthood, tissues such as the mammary, prostate, salivary and sweat glands are also believed to self-organize into the correct architecture through a hierarchy of cell-cell cohesive interactions (9, 31). However, the cells in these and other adult tissues must dynamically regulate their cohesivity and motility to serve specialized

roles at different locations and at different times. For example, the inner luminal (LEP) and outer myoepithelial (MEP) cells of the mammary gland are enormously plastic, undergoing physical and chemical changes throughout development, estrous cycles, pregnancy, involution and the early stages of malignant disease. In the mouse, for example, elevated cell motility at the terminal endbud is associated with lumen filling, changes to cell cohesion, and differences in cell motility (32-35). During these dynamic processes, transient disruption of cell positioning can occur concomitant to changes to the ordered hierarchy of cell-cell cohesive interactions required for robust cell sorting, yet tissue architecture recovers rapidly (34, 35). The strategies used by the mammary gland and related tissues to self-organize and repair robustly when cell properties change as a function of time have not been identified. Furthermore, adult tissues also comprise populations of cells that can be heterogeneous in their molecular and physical properties at the steady state (38, 39). The mammary gland is a prototypical example of a heterogeneous tissue, possessing considerable spatial and temporal variability within both the inner luminal and outer myoepithelial populations. For example, neighboring cells in healthy tissue can differ markedly with respect to their expression of adhesion molecules, cytoskeletal proteins, hormone receptors, and signaling pathway activation (33, 40-45). When heterogeneity affects the distribution of cohesive properties among different cell types, it can confound the ordered hierarchy of interactions necessary to drive self-organization robustly (2). Despite this heterogeneity, LEP and MEP retain their relative positions within the gland efficiently. The strategies available to these and other heterogeneous populations of cells to self-organize robustly have also not been defined. We investigated the hypothesis that contextual cues provided by the tissue-ECM boundary render self-organization robust to

29

changing or heterogeneous cell-cell interactions. We begin by reconstituting the self-organization of the human mammary epithelium (or related tissues) starting from aggregates of primary MEPs and LEPs in the presence or absence of ECM.

3. Methods

3.1. General materials and methods

Agarose was obtained from Allstar Scientific (490-050; Lot # 1004VIVCN) and used at a concentration of 3% (w/v) in PBS. Different concentrations of agarose or different non-adhesive hydrogels such as polyethylene glycol (PEG) and polyacrylamide (PA) reproduce the same experimental outcome we describe for HMEC without affecting kinetics (data not-shown). Matrigel was obtained from BD Biosciences (354230; Lot # 07898) and was used without dilution. Different Matrigel Lot numbers or different formulations of adhesive gels (e.g. Collagen-Matrigel mixtures) reproduce the same experimental outcomes we describe but can alter the kinetics of self-organization (data not shown). In general, higher concentrations of Matrigel or added collagen increase the speed of self-organization. A typical self-organization experiment begins by isolating luminal or myoepithelial (basal for prostate) cells from primary human tissue cultures or directly from human tissues via FACS. After sorting, these cells are reconstituted in agarose or Matrigel using photolithrographically defined microwells, DNA-mediated programmed assembly,

or Sacrificial Micromolding. Alternatively, one can pre-aggregate cell-clusters in agarose microwells and then transfer them to Matrigel. However, these transfers must be preformed rapidly before patterns of self-organization emerge. It is also important to notice that some of the methods used for these studies have been already described in chapter 1 and are not entirely reported in this section.

3.2. Human Mammary Epithelial Cells

Cultured normal finite lifespan primary HMEC were obtained from reduction mammoplasty tissue of a 19 year old individual (specimen 240L) and cultured in M87A medium with cholera toxin and oxytocin as previously described (46). All cultured primary HMEC were used for experiments at passage 4. Uncultured primary HMEC were directly isolated from organoids of 23, 16, and 19-year old individuals (specimens 59L, 160L, and 168 respectively). Dr. Martha Stampfer at LBNL provided all HMEC used in this study as de-identified human material.

3.3. Isolating LEP and MEP from primary HMEC and cultured primary HMEC

Primary human mammary epithelial cells at passage 4 were established and maintained in M87A medium according to previously reported methods (46). To lift the cells prior to sorting, a 10 cm dish was rinsed with PBS (Calcium and Magnesium free) with 0.04% EDTA and then incubated with PBS (Calcium and Magnesium free) with 0.04% EDTA at 37 ˚C until cells were rounded with a few detaching from the substrate.

The PBS (Calcium and Magnesium free) with 0.04% EDTA was then transferred to a collection tube and replaced with 1.0 ml of 0.05% trypsin for 30-60 seconds at 37 ˚C. The flask was then tapped sharply to dislodge the remaining cells and the cells were collected in M87A medium. Cells were counted and pelleted at 160 x g for 4 minutes. Pelleted cells were washed once more with PBS and resuspended in growth medium at a concentration of 10^7/ml. Fluorescently tagged antibodies for CD10 and CD227 were then added to the cells at the dilution reported in Table 1 and incubated for 30 minutes on ice. Finally, labeled cells were washed three times with PBS to remove unbound antibody and resuspended in FACS buffer (PBS containing 2 % BSA, 1 mM EDTA, and 1 µg/mL DAPI). Cells were then sorted on a BD FACSAria II controlled by FacsDiva software. LEPs were gated as a population of CD227+/CD10- (Muc1+/Calla-) cells, MEPs were gated as CD227-/CD10+ (Muc1-/Calla+) cells as shown in fig. S1A. For uncultured primary HMEC, cryogenically preserved organoids were thawed and collected into a 50 ml tube. The organoids were then washed in PBS to remove freezing medium and resuspended in 5 ml of 0.25 % trypsin with saline and EDTA. Organoids were incubated with gentle agitation at room temperature for 10 minutes and then shaken vigorously for 30 seconds. 10 ml of cold M87A medium was added to inhibit trypsin activity and the cell suspension was filtered through a 40 µm mesh cell strainer to remove aggregates and debris. Cells were pelleted at 300 x g for 4 minutes and resuspended at a concentration of 10^7/ml in ice cold M87A medium, stained with CD227 and CD10 antibodies as described above, and FACS purified as shown in fig. S1B.

3.4. Human Prostate Epithelial Cells (HPEC)

All primary human prostate epithelial cells were obtained from the Urology Department of Stanford University following an Institutional Review Board approved protocol and in collaboration with the Laboratory of Dr. Donna Pheel. The procedure for isolating and reconstituting luminal and basal epithelia from primary prostate tissue was similar to the one described for primary mammary tissue. However, these experiments required different reagents, antibodies, media-formulations, and an additional surgical step designed to isolate healthy prostate tissue from cancerous tissue immediately after the prostectomy surgery. For instance for the benign left side of prostate sample MB (right side bearing a Gleason Score 3+3 tumor), 8-mm cores were removed and submerged in ice-cold HEPES-buffered saline (HBS) using an automated coring device (Alabama Research and Development, Mundford, AL) under aseptic conditions. A Krumdieck tissue slicer (Alabama Research and Development) was then used to prepare precision-cut 300 μm thick tissue slices as previously described (47). 80 tissue slices were first washed with HBS in a sterile 5 mm dish, and then Collagenase (200 U/ml) was added in addition to MCDB 105 medium with 50 nM R1881 (Sigma), 10 μM Y27632 (Sigma) and 2 U/ml Dnase I (Amp. Grade, Invitrogen) (48). The tissue was minced with sterile scissors into small pieces (<1 mm^3) and pipetted vigorously. While in collagenase digestion medium, the sample was transported on ice from Stanford to UCSF. Immediately upon arrival to UCSF, the chunks of tissue were inserted in a rotator shaker and incubated at 37 ˚C (Note: For this particular sample, there were eight 15 mL conical tubes with 10 tissue slices/tube). After overnight digestion, the tissue suspension in each conical tube was pelleted and incubated with 5 mL of 0.2 % Trypsin/0.2 % EDTA (per tube) for 10 min at 37 ˚C before quenching with 10 mL

of soybean trypsin Inhibitor (Cascade Biologics). The digested tissue was then strained through a 40 µm filter, pelleted, and resuspended in HEPES buffer. All tissue suspensions were combined in a single conical tube and placed on ice. At this point the cell count was approximately 23×10^6. These cells were pelleted and resuspended in 2.3 mL of DMEM (for an approximate concentration of $1 \times 10^6/100$ µL). 50 µl of the cell suspension were dispensed in 3 FACS tubes and incubated with either nothing (unstained "control"), 2.5 µL of APC-conjugated CD44 antibody, or 10 µL of FITC-conjugated CD57 antibody (Table S1 for details). The remaining cell solution was incubated with both antibodies (460 µL of anti-CD57 and 115 µL of anti-CD44) following the manufacturers' suggestions for the desired concentration per test. After 30 min incubation on ice, the cells were diluted in DMEM (0.5 mL for the controls and 20 mL for the double stained cells), pelleted, and resuspended in 0.5 mL (for controls) or 1 mL (for double stained cells) of FACS buffer (1:1 DMEM/F12 with 1 ug/mL DAPI). The cells were finally strained one last time through a 40 µm filter and brought to UCSF's Laboratory for Cell Analysis (LCA) for sorting on a FACS AriaII instrument.

3.5. Cell staining using cytosolic or membrane dyes

For cell-substrate contact angle measurements, sorted LEPs or MEPs in 1 mL of PBS were separately stained with 5 µL of either DiI (Invitrogen Vybrant Multicolor cell-Catalog Kit V22889) for MEPs or 5 µL of DiO (Invitrogen Invitrogen Vybrant Multicolor cell-Catalog Kit V22889) for LEPs for 10 minutes at 37 ˚C, pelleted, and resuspended in M87A medium at the concentration defined for this assay. For all other assays, sorted LEPs or MEPs were suspended in 10 mL of PBS and incubated with either 1 µL of either 10 µM Cell Tracker Green (CTG, Invitrogen) for LEPs or 1 µL of 10 µM Cell Tracker Red (CTR, Invitrogen) for MEPs for 5 minutes at 37 ˚C, pelleted, and resuspended at a concentration of 10^7/ml in M87A. Although the membrane dyes gave crisper images than the cytosolic trackers, these were observed to be more toxic. Therefore, DiI and DiO were only used for our cell-substrate contact angle assays. Over the course of few hours, both the membrane (DiI and DiO) and the cytosolic (CTG and CTR) dyes tend to remain homogeneously diffused throughout the surface or the interior of HMECs and allow us to visually exclude those cells that did not recover from the experimental manipulations (e.g FACS, transfections, etc.) required for our assays.

3.6. Loading and visualizing lineage-specific cells in agarose

Homotypic or heterotypic populations of stained or unstained cells were centrifuged into the wells at 160 x g for 4 minutes. Excess cells were then washed away with medium and the remaining physically confined cell-aggregates were monitored for self-organization patterns by time-lapse microscopy or by immunofluorescence. Agarose was chosen as the non-fouling hydrogel material of choice because it is extremely cheap and easy to prepare. To micromold agarose we used a similar strategy to the one discussed for gelatin in chapter 1.

3.7. DNA Programmed Assembly

The chemical strategies used to encapsulate cell-aggregates in Matrigel were adapted from previously reported methods (49-52).

3.8. Sacrificial Micromolding

The physical strategies used to encapsulate cell-aggregates in Matrigel are described in chapter 1 and reported in reference 4.

3.9. Immunofluorescence

All microtissues were fixed with 4% PFA for 20 minutes and then incubated in blocking buffer (10 % heat inactivated goat serum in PBS + 0.5 % triton X-100) at 4 ˚C for at least 1 day. Primary antibodies were then diluted in blocking buffer and added to the sample as summarized in Table 1. After at least one day incubating at 4 ˚C with the primary antibody, all microtissues were washed several times with PBS + Tryton X for at least one day and incubated with alexa-conjugated secondary antibodies diluted at a concentration of 1:200 in blocking buffer for approximately 1 day. Before imaging the clusters, all sample were washed with PBS + 1 ug/mL DAPI for at least 1 hour.

Antibody	Product	Application
Anti-human Keratin 5	NeoMarkers XM26 (clone XM26)	IF (1:30)
Anti-human Keratin 8	Epitomics 1925-1 (poly)	IF (1:100)
Anti-human Keratin 19	Sigma C6930 (clone A53-B/A2)	IF (1:50)
Anti-human Keratin 14	Thermo RB-9020-P (poly)	IF (1:50)
Anti-human CD324	BioLegend 324112 (clone 67A4)	IF (1:100)
Anti-human Laminin 5	Millipore MAB19563 (clone D4B5)	IF (1:50)
Anti-human CD49f	Millipore MAB1378 (clone GoH3)	IF (1:50)
Anti-human CD227	BD 559774 (clone HMPV)	IF (1:50)
Anti-human Desmoglein 2	Novus NBP1-857096 (poly)	IF (1:50)
Anti-human Keratin 14	NeoMarkers XM26 (clone XM26)	IF (1:30)
Anti-human CD227-FITC	BD 559774 (clone HMPV)	FACS (1:50)
Anti-human CD10-APC	Biolegen 312210 (clone HI10a)	FACS (1:200)
Anti-human CD44-APC	BD 560532 (clone G44-26)	FACS (1:20)
Anti-human CD230-FITC	BD 555619 (clone NK-1)	FACS (1:5)
Anti-human CD49f-PE	Biolegend 313612 (clone GoH3)	FC (1:200)
Anti-human CD29-PE	Biolegend 555443 (clone T52-16)	FC (1:200)
Anti-human p120-catenin	BD 610133 (clone98/pp120)	WB (1:1000)
Anti-human Talin1	Cell Signaling 4021 (poly)	WB (1:500)
Anti-human β-catenin	Cell Signaling 8480 (clone D10A8)	WB (1:1000)
Anti-human β-actin HRP	Abcam ab49900 (clone AC15)	WB (1:2000)

Table 1. List of antibodies used, product numbers, and applications (IF – Immunofluorescence; FACS – Fluorescently activated cell sorting; FC – Flow Cytometry; WB – Western Blot). The dilution used for each application is reported in parenthesis.

3.10. Quantifying self-organization

To quantify the self-organization of HMEC in agarose or Matrigel we adopted three approaches. We termed the first approach Visual Scoring. Here, we inspect each reconstituted micortissue using phase and fluorescent microscopy and count the frequency of each self-organization pattern (i-v) as shown in Figure 2C. The advantage of this method is that we can count a large number of tissues and we can appreciate the subtle differences between all biological architectures. The disadvantage is that this method is subject to human bias. To mitigate this limitation we assigned criteria for Visual Scoring as follows: (i) – correct: 75-100% MEP coverage of a LEP core; (ii) – almost correct: 50-75% MEP coverage of a LEP core; (iii) – almost inverted: 50-75% LEP coverage of a MEP core; (iv) – inverted: 75-100% LEP coverage of a MEP core; (v) – scrambled: 2 or more phase transitions between MEPs and LEPs. The second quantification tool we use is the visualization of the average Cell-Tracker fluorescent intensity signals we collected imaging different microtissues (see Fig. 2B). These projections can be thought as Heat Maps that display in green and red the probability of finding LEPs and MEPs at that particular location in the reconstituted tissue. This quantification method does not introduce human bias but can be compromised by image-processing artifacts. Furthermore, the final average fluorescent projections do not capture all of the biological architectures we see when looking at the raw data. Our third approach is to plot the average localization of lineage-specific (i.e. luminal or basal) keratin intermediate filaments within a reconstituted tissue. This quantification requires collecting several high-magnification confocal images of fixed and stained structures, cropping the images to the exact size of the spherical tissue, binarizing the fluorescent signal from the green (for Keratin 19) and red (for Keratin 14)

channels, stacking (and resizing to smallest sample) all images collected, and plotting the normalized average (K14 and K19) signals as a function of the normalized radial distance from the center of an average spherical reconstituted microtissue as shown in Figure 1. Although this Keratin Profiling approach is the most quantitative method, it is time-consuming and may reflect biological processes (e.g. cell-differentiation) that relate but do not exclusively represent the contribution of self-organization to structure formation. When possible, we use all three approaches to quantify self-organization. All image analysis was accomplished in FIJI.

3.11. Functionalization of agarose microwells

To functionalize the free hydroxyl functional groups on agarose molds we washed the molds 2 times with 0.1 M sodium carbonate at pH 8.5 (coupling buffer) and then 2 M sodium carbonate (activation buffer). Activation of hydroxyl groups was initiated by adding 5 M cyanogen bromide in acetonitrile for ~2 mins at room temperature. Activated molds were subsequently washed with 1 mL of ice-cold deionized water and 1 mL of coupling buffer. Finally, wells were treated with either 2 mg/mL BSA, 0.5 mg/mL ECM protein, or no protein in coupling buffer overnight at 4 ˚C. The wells were then given a fresh solution of protein in PBS for another incubation period of 24 hours at room temperature. On the day of the experiment, any residual reactive groups were blocked by treating the wells with 50 mM ethanolamine (pH 9.0) for 1 hour prior to copiously washing off the molds with M87A medium for several hours at room temperature. The ECM

proteins used for the results presented in Figure 4 were Fibronectin 1 (Sigma F1141) and Collagen 1 (Advanced Biomatrix 5005-B).

4. Results

4.1. Human mammary epithelial cells can self-organize into an inverted architecture in the absence of extracellular matrix.

During self-organization, cells can take cues from each other and the surrounding microenvironment to guide their ultimate position in the tissue. To start defining the relative contributions of cell-cell and cell-ECM interactions on cell positioning in the mammary gland, we reconstituted aggregates of human mammary epithelial cells in the presence and absence of ECM. We used luminal (LEP; Muc1+, Cala-) and myoepithelial cells (MEP; Muc1-, Calla+) isolated via FACS from fourth passage cultures of human reduction mammoplasty tissue. These purified populations of cultured primary cells were reconstituted at 50:50 ratios, either fully embedded within 3D reconstituted basement membrane gels (Matrigel), or in non-fouling microwells (agarose). As briefly discussed in the chapter 1, LEP and MEP efficiently formed the correct architecture in Matrigel after 24 hours. Strikingly, however, these same cells self-organized into an inverted architecture in agarose (Fig. 1). In this inverted architecture, LEPs were positioned at the tissue periphery, with MEPs forming a tight aggregate in the tissue core.
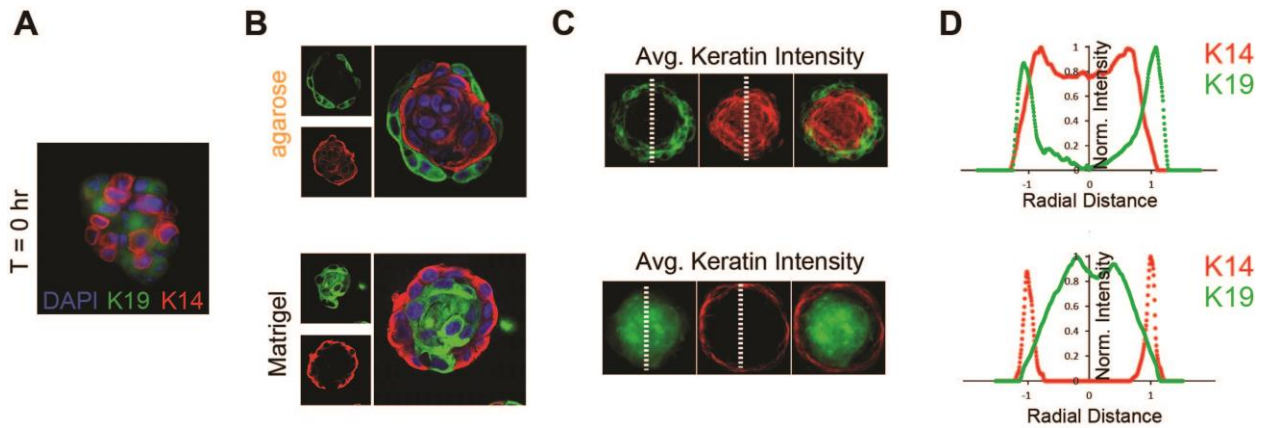
Figure 1: In the absence of ECM, human mammary epithelial cells can Self-Organize into an inverted architecture. (A) 40X Confocal microscopy image of a heterotypic aggregate of LEPs and MEPs fixed and stained for keratin markers (K14 for MEPs and K19 for LEPs) immediately reconstitution. **(B)** Representative 40X confocal microscopy images of a microtissue stained for K14 (red), K19 (green), and Cell nuclei (blue) after 1 day in agarose (top) or Matrigel (bottom). **(C)** Average K14, K19, and merged profiles for 15 different HMEC clusters after 24 hours in agarose (top) or Matrigel (bottom). **(D)** Normalized average keratin intensity profiles as a function of normalized radial distance for the data presented in C. All spherical microtissues had an approximate diameter of 100 μm.

These changes in tissue architecture could not be attributed to differentiation, as identical results were observed with purified LEP and MEP stained with live cell tracking dyes prior to reconstitution (Fig. 2). Therefore, cues derived from the surrounding matrix can quantitatively convert an inverted tissue configuration into one with the correct topology.
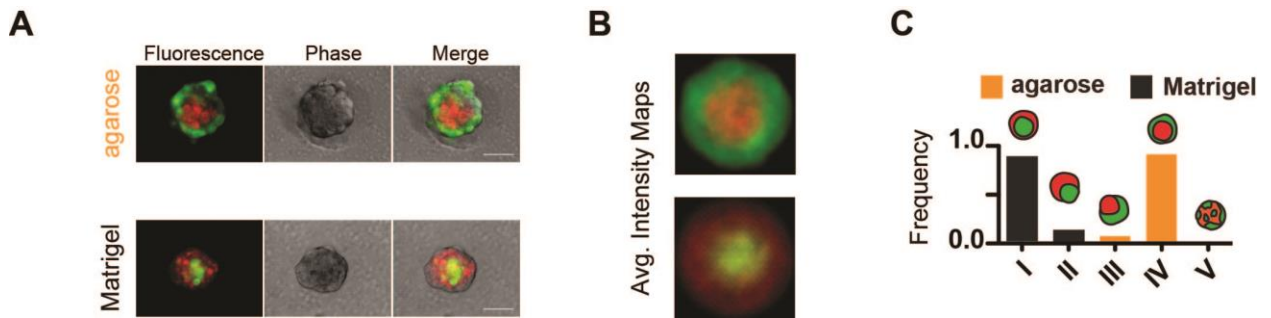
Figure 2: Self-Organization is not differentiation. (A) Representative 40X phase and fluorescent images of heterotypic aggregates of LEPs (green) and MEPs (red) stained with Cell Tracker Green (CTG) and Cell Tracker Red respectively and after 24 hours in agarose microwells (top) or in Matrigel (bottom). **(B)** CTG and CTR average intensity projections for 30 HMEC clusters after 1 day in agarose (top) or Matrigel (bottom). **(C)** Visual Scoring for HMEC clusters after 1 day in agarose (N= 268; top) or Matrigel (N= 235; bottom).

After proper self-organization in Matrigel, many tissues went on to polarize and form lumen after an additional 72 hours (see Fig. 3). Interestingly, none of the tissues that were reconstituted in agarose exhibited patterns of proper polarization and structure formation. This suggests that only the correct cellular topology promotes lumen formation.
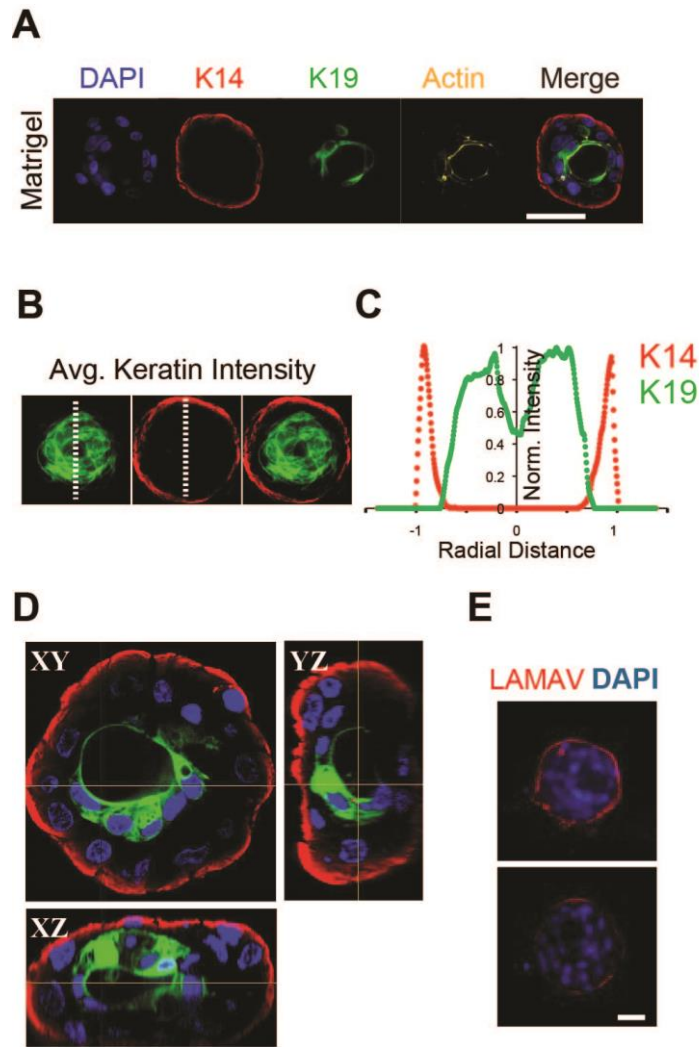
Figure 3: Lumenization or reconstituted HMEC. (A) Sample 40X confocal microscopy images of a lumenized HMEC cluster stained for K14 (red), K19 (green), actin (yellow) and nuclei (blue) after 96 hours in Matrigel. **(B)** Average K14, K19, and merged intensity profiles for 9 different lumenized HMEC clusters after 96 hours in Matrigel. **(C)** Normalized average radial keratin profiles for data in B. **(D)** Orthogonal confocal views of a sample lumenized acinus fixed and stained for K14 (red), K19 (green) and cell nuclei (blue). **(E)** Sample 20X confocal microscopy images of lumenized acini fixed and stained for Laminin V (red) and DAPI (blue). All Scale bars are 50 μm.

4.2. Matrigel provides a substrate for the assembly of a self-generated adhesive cue at the tissue-ECM boundary

Matrigel could alter tissue architecture by providing specific diffusible signals to the organizing cells, by providing specific basement membrane components, or by acting as a substrate for the tissue to assemble its own basement membrane at the aggregate-Matrigel boundary. To test whether Matrigel provides specific diffusible factors or basement membrane components to the tissue, we repeated the self-organization assay in agarose microwells covalently functionalized with Collagen-I (COL1) or Fibronectin-I (FN1) – two ECM proteins that are only minor constituents of Matrigel (13, 14). Both COL1- and FN1-functionalized agarose effectively redirected MEPs from the tissue core to the periphery, suggesting that Matrigel likely functions by providing a substrate for the assembly of a basement membrane (Fig. 4). Consistent with this notion, these purified ECM components were also unnecessary to drive MEP to the tissue boundary, as we observed similar results using PDMS microwells, a non-biological material that was observed to physisorb secreted basement membrane proteins such as Fibronectin-1. In contrast, other non-biological but non-fouling hydrogels such as PEG-acrylate or polyacrylamide did not direct MEP to the tissue boundary (not shown). Together with the observation that basement membrane components were also deposited at the MEP-Matrigel boundary, these observations suggested that Matrigel, PDMS, and functionalized agarose act to reorganize tissue architecture by providing an interface at the tissue boundary where cells can assemble their own adhesive basement membrane. As discussed in Chapter 1, however, in PDMS the cells only transiently achieved a properly organized conformation that could not be maintained for subsequent polarization and structure formation. In

functionalized agarose, the structures maintain the correct cellular topology longer than in PDMS. However the physicochemical properties of 3% agarose functionalized with Fibronectin1 or Collagen 1 did not promote subsequent morphogenesis.
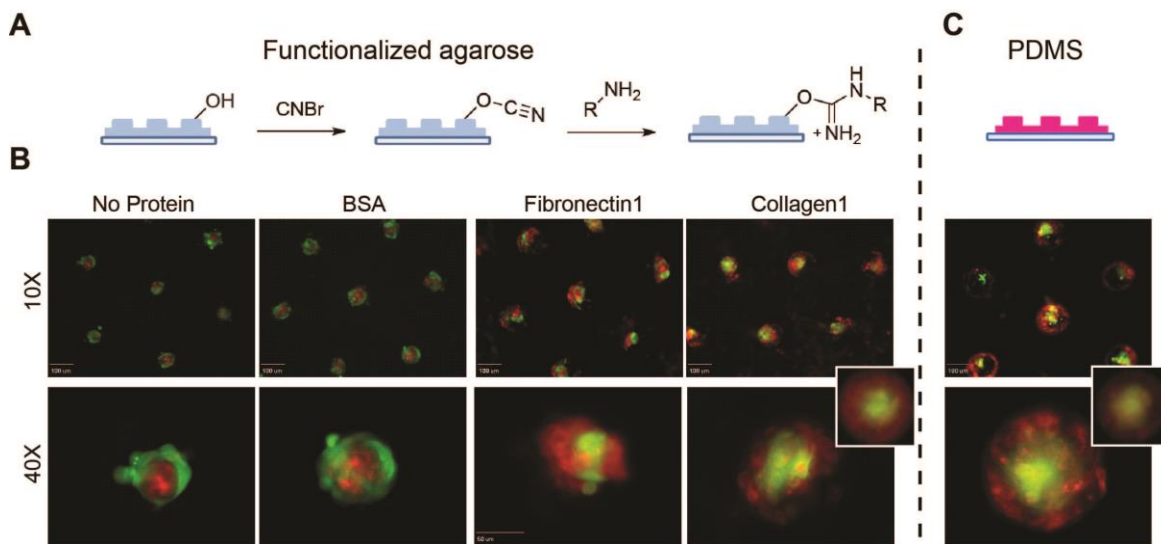
Figure 4: Self-Organization of HMECs in functionalized agarose and PDMS microwells. (A) Schematic representation cyanogen bromide activation and functionalization of agarose surfaces. **(B)** 10X and 40X representative images of LEPs and MEPs stained with CTG and CTR, respectively, and allowed to self-organize for 24 hr in cyanogen bromide treated agarose microwells functionalized with no protein (i.e. ethanolamine), Bovine Serum Albumin (BSA), Fibronectin1, or Collagen1 (left). The inset is an average intensity projection of 30 clusters. **(C)** Representative images of LEPs and MEPs stained with CTG and CTR after 24 hr in PDMS microwells. The inset is an average intensity projection of 30 clusters.

4.3. In the presence of a strong tissue-ECM boundary, Self-organization of human glandular tissues is robust to highly variable cell-cell interactions

We repeated the agarose vs. Matrigel assay using uncultured primary human cells directly isolated from reduction mammoplasty tissue (i.e. Passage 0 cells). Compared to the fourth passage cells used in our previous experiments, these uncultured primary cells have elevated levels of cellular heterogeneity in a variety of cell-surface markers (42, 53) and, as we will discuss in chapter 3, have a higher underlying variability in the energetics of cell-cell interfaces. Nevertheless, also these cells self-organized robustly in Matrigel. However, the same was not true in agarose, where self-organization can only occur through cell-cell interactions alone, and where many tissues organized into indeterminate or only partially inverted architectures (Fig. 5).
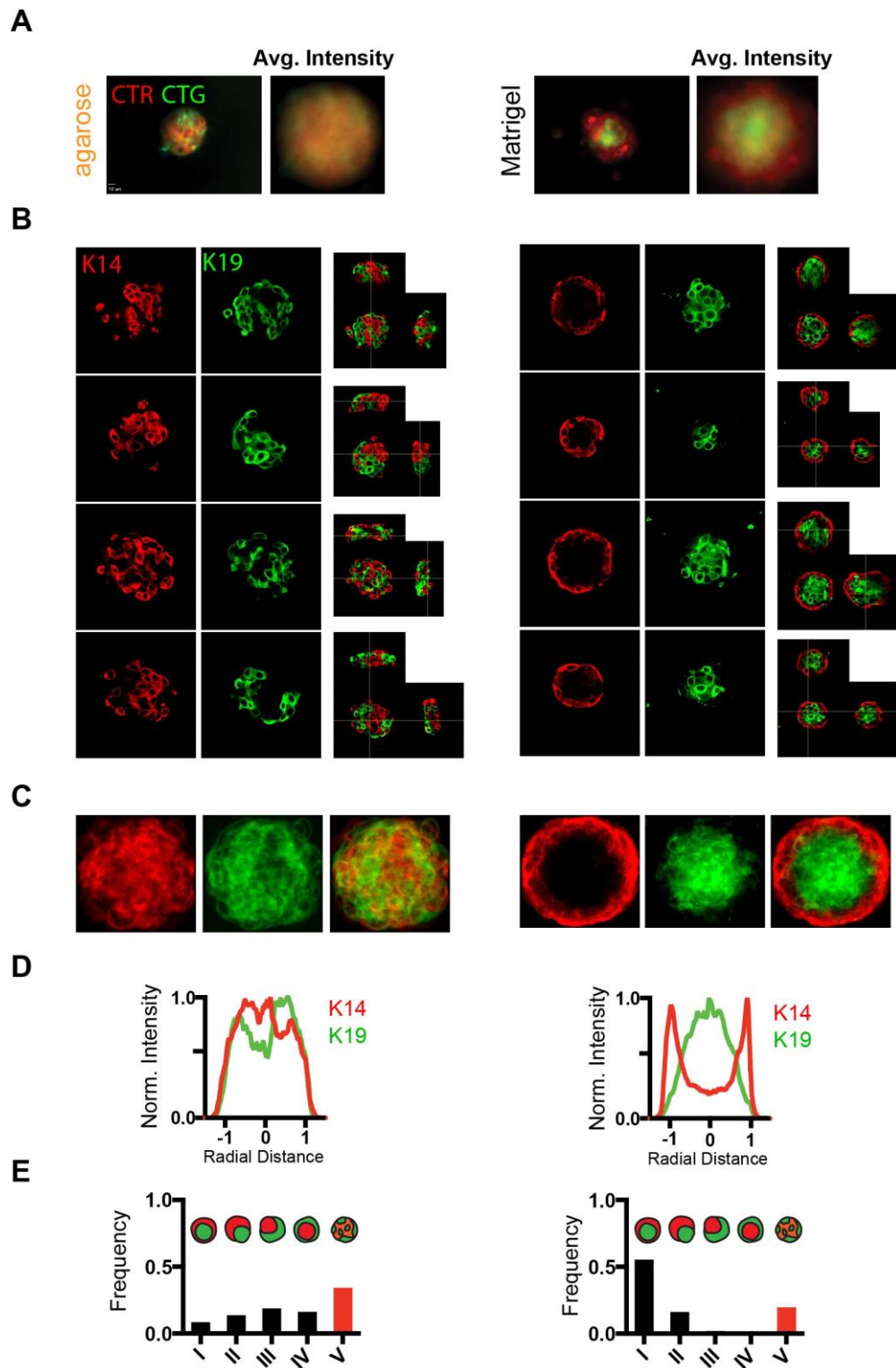
Figure 5: Self-organization of uncultured primary HMEC in agarose and Matrigel. (A) Representative

40X epifluorescence microscopy image and average fluorescent intensity (N=18) of LEPs and MEPs in

agarose (left) or Matrigel (right) (green = LEP, Cell Tracker Green; red=MEP, Cell Tracker Red). Scale bar = 10 μm. **(B)** Representative 40X confocal microscopy images and orthogonal reconstructions of primary LEPs and MEPs after 24 hr in agarose (left) and Matrigel (right) (green = K19; red = K14) Scale bar = 10 μm. **(C)** Average K14 and K19 intensity for 13 primary HMEC clusters after 24 hr in agarose (left) or Matrigel (right). **(D)** Normalized average keratin radial intensity plot for primary HMEC (N=13) derived from sample 59L after 24 hr in agarose (left) or Matrigel (right). **(E)** Average visual scoring of primary HMEC clusters derived from two additional donors (samples 160L and 168) after 24 hr in agarose (N= 39; left) or in Matrigel (N= 28; right).

These results were generalizable to other human tissues sharing the architecture of the mammary gland. For example, populations of uncultured and healthy basal and luminal cells isolated from human prostatectomies were found to self-organize efficiently in Matrigel, but not in agarose. Remarkably, the rules of self-organization for the mammary and prostate also seemed to be cross compatible, and thus entirely independent of tissue-specific cell function. For example, we found that healthy basal prostate cells retained strong ECM adhesion and self-organized robustly with cultured luminal mammary epithelial cells that lacked cell-ECM adhesion (Fig. 6). For these experiments it is important to emphasize that self-organization only refers to the relative positioning of the cells within the tissue.
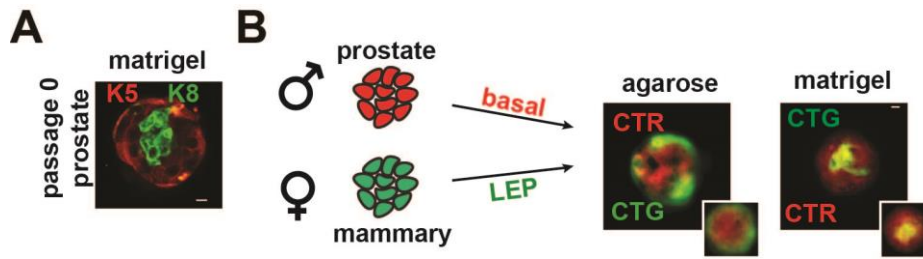
Figure 6: Self-Organization of HPEC. (A) Representative image of self-organized uncultured primary basal and luminal cells derived from a human prostectomy surgery after 24 hours in Matrigel. **(B)** Self-organization of primary prostate basal cells with primary luminal mammary epithelial cells after 24 hours in agarose or Matrigel.

5. Discussion

The prevailing intellectual framework for understanding why dissociated embryonic cells will spontaneously reorganize into structures resembling normal organs (3) was largely developed by Steinberg in the 1960s and 1970s and was proposed to rely almost exclusively on homotypic and heterotypic adhesive properties of different cellular groups. This DAH model has withstood considerable experimental validation, including in situations where the adhesive properties of the cells were well controlled (54). However, the results presented in this chapter clearly show that the ECM can dramatically alter the outcome of the self-organization process by providing an additional interface for cell adhesion.

Therefore, in order to improve the conceptual understanding of cell-sorting in tissues with extensive extracellular matrix, we must try to compare the relative cell-cell and cell-ECM interactions of each cell type. In chapter 3, we present and discuss a series of experiments that quantify cell-cell and cell-ECM adhesions of LEPs and MEPs to them selves, each other, and the ECM. In chapter 4 we use these measurements to estimate the relative works of adhesion between MEPs, LEPs and the ECM in order to build a mathematical model that predicts the self-assembly of these cells *in vitro*. The model highlights the importance of the geometric constrains of a tissue and provides a fundamentally novel conceptual framework for understanding tissue self-assembly. It also allows us to predict the outcome of cell sorting under conditions that we can experimentally test. This will allow us to investigate the architectural consequences of oncogenic mutations that trigger cell-cell and cell-ECM adhesion aberrations, and to explore the robustness of each tissue conformation in response to dynamic cellular perturbations or cellular variability.

Chapter 3

Quantifying Cell-Cell and Cell-ECM adhesion at the molecular, cellular, and multicellular level

1. Introduction

The observation that the tissue-ECM boundary provides an additional adhesive interaction driving tissue self-organization prompted us to quantify the hierarchy of cell-cell cohesive and cell-ECM adhesive interactions among mammary epithelial cells. To do so, we performed a series of experiments that allowed us to analyze the morphometric differences of cells in contact with other cells or a surrogate ECM substrate. As the interfacial tensions at the cell-cell, cell-substrate, and cell-medium interfaces direct the spreading of the cell cortex, we use cell-cell and cell-ECM contact angle, circularity, and spreading assays to evaluate the relative strength of each interaction at the cellular and multicellular level. In addition, we perform qPCR screens in order to relate these physical measurements to the molecular characteristics of LEP and MEP. In this chapter we present experimental evidence supporting the notion that in human glandular epithelia such as the prostate or mammary gland, the adhesion of the basal cell-type to the ECM is the most important interfacial phenomena contributing to the self-organization of reconstituted MEPs and LEPs into microtissues that exhibit the *in vivo* cellular topography.

2. Background

Cells cannot be considered inanimate objects that reach thermodynamic equilibrium. However, contact angles can still relate to the balance of interfacial forces that a cell is experiencing. Therefore, several instruments such as AFMs or microaspirators have been used to bring two cells or a cell and a surface in contact in order to measure the angle formed at that interface (55). We decided to measure MEP-LEP, MEP-MEP, or LEP-LEP contact angles by accommodating cell doublets in small non-adhesive rectangular microwells in order to minimize the cellular manipulations required by other techniques such as microaspiration. For cell-ECM contact angle measurements, we simply deposited cells onto Matrigel coated substrates and used confocal microscopy to visualize the interaction of cells with the surrogate ECM.

After comparing the relative contact angle for all combinations of MEP, LEP and ECM, we asked whether these measurements translated to the multicellular level. To do so, we measured the circularity of multicellular cell-aggregates as a function of time and the spreading area of cell-aggregates onto the Matrigel-coated substrate. We found that the hierarchy of adhesion at the single cell level translated to the multicellular level and correlated with the molecular properties of these cells.

3. Methods

3.1. Cell-Cell contact angle measurements

FACS-sorted HMECs stained with either Cell Tracker Green or Cell Tracker Red were centrifuged into small rectangular agarose microwells (20 μm x 40 μm x 15 μm) fabricated using the photolithography and micromolding methods described above. Wells were designed to accommodate two cells. After 4 hr in the wells, the cell doublets were imaged at 40X magnification and analyzed in FIJI in order to determine the contact angle at the cell-cell interface. For these experiments we visually screened for microwells that contained cell doublets that were alive and contained 2 cells of comparable size.

3.2. Cell-ECM contact angle measurements

Glass coverslips were submerged in a solution of Matrigel diluted in M87A (1:50 v/v) on an orbital shaker at room temperature. After overnight adsorption of Matrigel protein components, the coverslips were rinsed with PBS and incubated for few hours with a solution of 4 nM QD605 (Invitrogen) in M87A to assist in resolving the interface. These coverslips were then washed with M87A and used as substrates for the spreading of FACS-sorted LEPs and MEPs stained with either DiI or DiO as previously described. To measure the contact angle at the cell-substrate interface, we analyzed 60X confocal Z-stacks in FIJI. For these experiments we visually screened for cells that were spreading onto the surfaces in a symmetric fashion and that were not interacting with nearby cells.

3.3. Cell-aggregate circularity and Cell-cluster spreading

For measuring the circularity of homogenous LEP or MEP clusters we loaded agarose microwells as described above and allowed the cells to interact overnight before collecting multiple images for each condition at 40X magnification. The contours of the microtissues were then extracted from the image and analyzed for circularity scores using FIJI's built-in circularity measurement tool. This function defined circularity (*C*) as follows:

$$c = 4\pi * \frac{(Area)}{(Perimeter)^2}$$

For the spreading assay of LEP and MEP-clusters over Matrigel-coated substrates we transferred the cell-aggregates after 6 hours in agarose microwells onto glass coverslips treated as described for the Cell-ECM contact angle measurements. These clusters were then allowed to spread on the substrate for 12 hr before being fixed and stained for lineage-specific keratin markers and then analyzed for the extent of tissue-matrix interactions via phase contrast or confocal microscopy. It is important to note that while all MEP-clusters were observed to interact with the substrate, most LEP-clusters were so non-adherent that they were removed during the immunofluorescence washing steps. We therefore interpret our measurements are considerable overestimates of LEP adhesion.

3.4. RT-PCR of HMEC MEP and LEP

Three different batches of fourth passage HMEC were FACS-sorted into LEP and MEP populations (on 3 different days). Immediately after sorting, RNA was isolated from the 2 cell populations using RNeasy Mini Kit (Qiagen 74104), converted to cDNA using a RT2 First Strand Kit (Qiagen 330401), mixed with QIAGEN's RT2 PCR master mix, and aliquoted across 2 SA-Biosciences PCR arrays (PAHS-146Z for cell-cell adhesion molecules and PAHS-013 for cell-ECM adhesion molecules); the target concentration of RNA loaded into each array was 2 µg. The plates were then run on an ABI Vii7A RT-PCR instrument. Built in positive and negative controls showed successful PCR amplification with no genomic DNA contamination. Identical threshold values for all MEP (n=3) and LEP (n=3) plates were used in order to extract raw threshold cycles (Cts) from the RT-PCR data. These raw Ct values were then used to calculate fold-changes using the ΔΔCt method. To normalize the data, we used the average of the arithmetic means of 3 genes: GAPDH, ACTB, and HPRT1. To interpret the data, the LEP population was used as the "control" (i.e. over or underexpression of MEP genes with respect to LEP genes) as shown in Figures 4 and 5. Genes not amplified by cycle 35 were considered undetermined. P-values were calculated using a Student's t-test. Data analysis was performed using the online software provided by SA BioSciences

4. Results

4.1. Cell-ECM adhesion is binary because only MEP adhere to the tissue-ECM boundary

In conjunction with measurements of interfacial surface area, contact angles provide a means of quantifying the relative "energy of interaction" between all components in the mammary epithelium. In our cell-cell contact angle assay, we reproducibly found that MEPs formed the most cohesive interactions, having the largest cell-cell interface as well as the largest contact angle (69 deg; Fig. 1D). This was followed by heterotypic MEP-LEP interactions (53 deg) and finally homotypic LEP-LEP interactions (45 deg). These measures of cell cohesion are consistent with the observation that MEPs organize in the tissue core in the absence of a ECM boundary (see Chapter 2), where the most cohesive cells would maximize their homotypic interfaces.

We next measured the contact angle between LEPs, MEPs, and a Matrigel coated substrate. The cell-ECM contact angle for MEPs was pronounced at 4 hr (Fig. 1E), and converged to a value of 119 deg after an additional 8 hours (not shown). This value was significantly larger than the contact angle at the MEP-MEP interface. More striking, however, was the observation that the vast majority of LEP were unable to interact with the Matrigel coated surface. Those few cells that interacted had an average contact angle near the lower limit of detection for the assay.
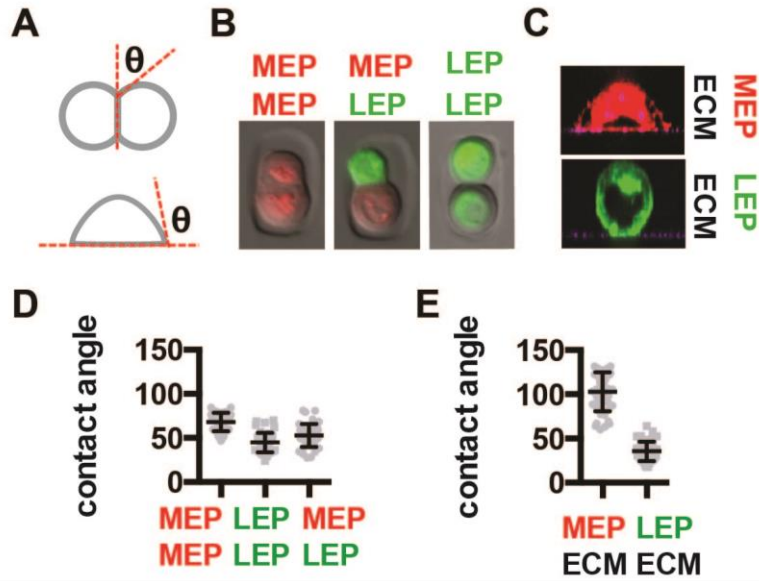
Figure 1: Cell-Cell and Cell-ECM contact angles. (A) Schematic illustration exhibiting our definition of contact angle at the cell-cell (top) or cell-ECM interface (bottom). **(B)** Sample images of cell doublets. **(C)** Sample XZ confocal projections of single cells on Matrigel coated glass used for measuring the contact angle at the cell-cell and cell-ECM interfaces. (green = LEP; red = MEP; purple = QD605). **(D-E)** Distribution of measured contact angles at all interfaces (n>42).

4.2. Binary Cell-ECM adhesion at the multicellular level

These properties of MEPs and LEPs were retained at the multicellular level, as more cohesive MEP aggregates had higher circularity then the less cohesive LEP aggregates (Fig. 2), yet preferentially spread on ECM coated surfaces (Fig. 3).
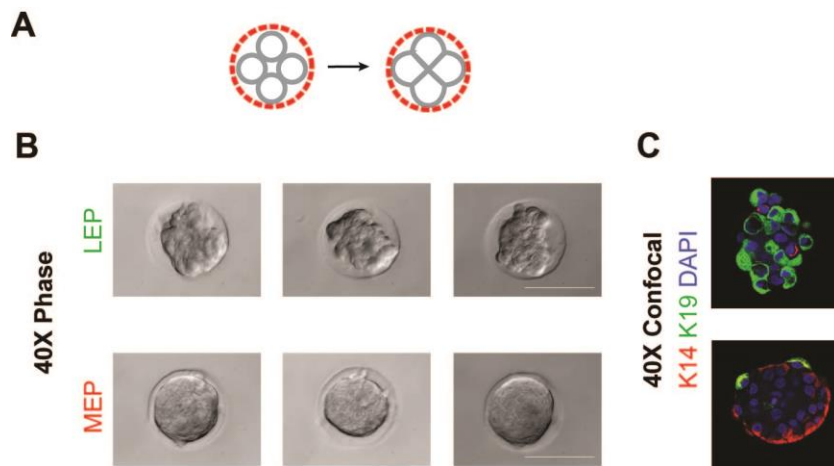
Figure 2: Circularity and cell-cohesion at the multicellular level. (A) Schematic representation of our circularity assay. **(B)** Sample images of aggregates of homogeneous MEP and LEP after 12 hours in agarose wells used for measuring circularity. **(C)** Sample aggregates fixed and stained for lineage-specific keratin markers. Scale bar = 100 μm.
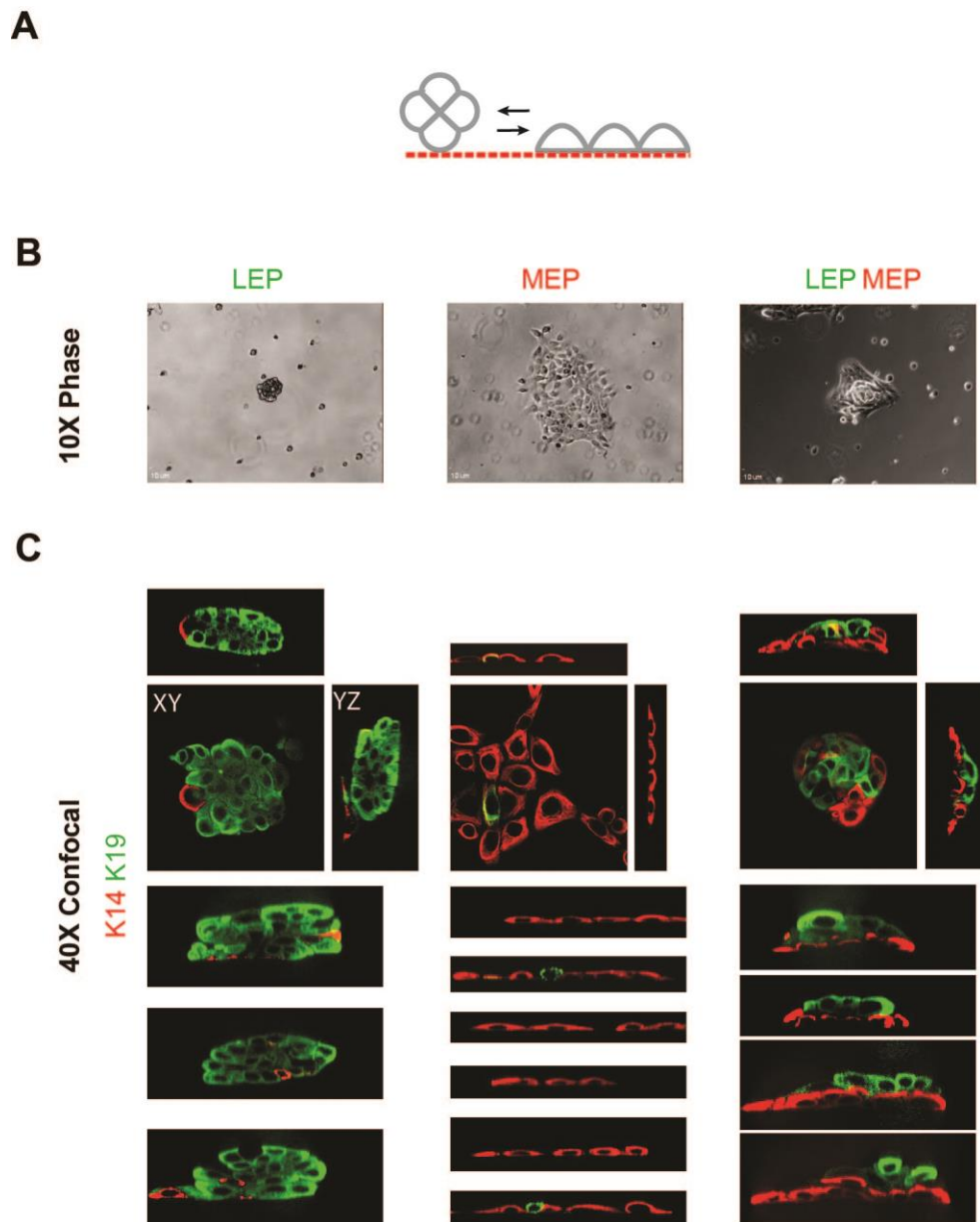
Figure 3: Cluster spreading and ECM adhesion at the multicellular level. (**A**) Schematic representation of our cluster-spreading assay. (**B**) 10X microscopy images of homotypic or heterotypic cell-aggregates after spreading on Matrigel coated coverslips for 12 hr. (**C**) 40X confocal microscopy images of homotypic or heterotypic cell-aggregates after spreading on Matrigel coated coverslips for 12 hr. K14 and K19 staining confirms the identity of each lineage. Scale bars are 10 μm.

4.3. Binary Cell-ECM adhesion at the molecular level

Adhesive differences between MEP and LEP were also reflected at the molecular level, where we found most components of the ECM adhesion machinery were over-expressed in MEP relative to LEP (Fig. 4). As many of these genes have been already identified as key markers of the basal cell-lineage (56), this was not surprising. On the other hand, the mRNA expression profile of genes known to regulate cell-cell adhesions were not found to be particularly over or underexpressed in MEP relative to LEP (Fig 5). Considering the previous literature suggesting the more cell-cell cohesive nature of LEPs (9, 31), this was somewhat puzzling.

A

Expression Level in MEPs; Log($2^{-\Delta Ct(MEP)}$)

Expression level in LEPs; Log($2^{-\Delta Ct(LEP)}$)

- In RED genes overexpressed in MEPs w.r.t LEPs
- In GREEN genes underexpres. in MEPs w.r.t LEPs

B

- Log10 (P-Value)

P-value = 0.05

-Log2(Fold Control of MEP/LEP)

C
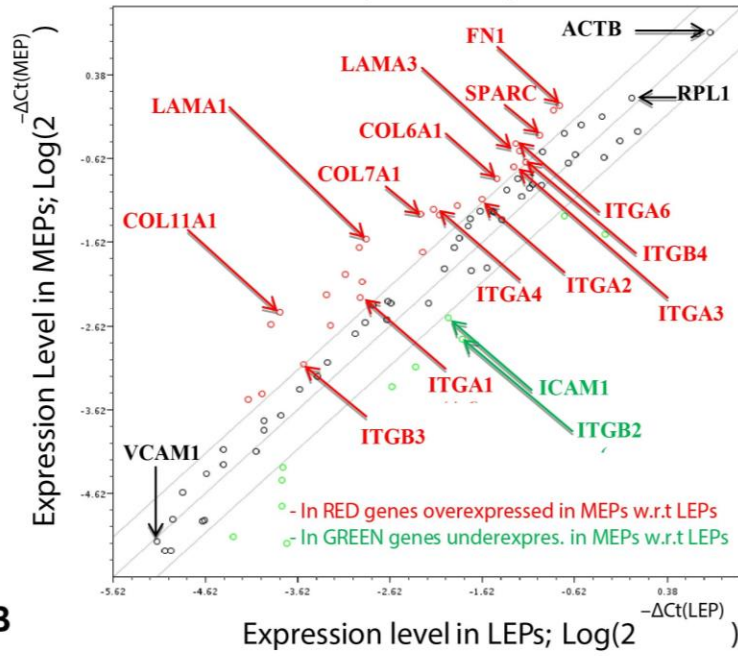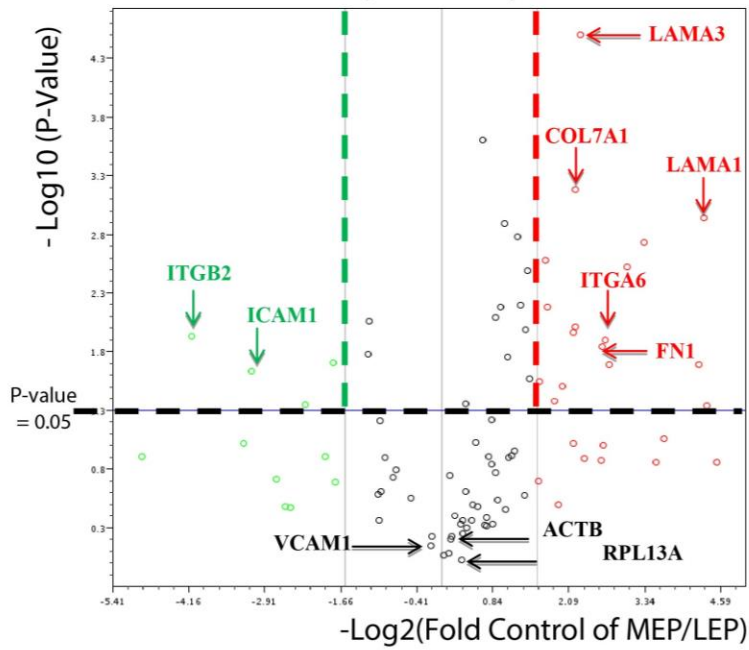
GENE	Fold Reg	P-Value
MMP3	20.58	0.045848
LAMA1	19.9	0.001156
MMP1	18.9	0.020323
COL7A1	10.07	0.001856
ITGA4	8.36	0.002981
THBS2	6.8	0.020468
ITGA6	6.5	0.012699
FN1	6.28	0.014437
LAMA3	4.85	0.000031
SPARC	4.63	0.000653
ITGA1	4.6	0.009826
KAL1	4.5	0.010793
COL6A1	3.96	0.031306
ITGA3	3.62	0.041596
COL5A1	3.34	0.006622
ITGA2	3.27	0.002634
ITGB4	3.06	0.02833
MMP7	-17.26	0.011632
ITGB2	-8.72	0.023136
MMP15	-4.73	0.045259
ICAM1	-3.43	0.019627
COL11A1	23.18	0.138137
MMP13	11.52	0.138647
COL16A1	6.22	0.133479
TIMP1	6.36	0.099112
ITGB3	3.02	0.201825
CD44	2.14	0.017713
VCAN	1.96	0.006662
ECM1	2.06	0.001285
ITGB1	1.6	0.000247
LAMA2	1.77	0.060047
LAMB1	2.38	0.001648
LAMB3	2.68	0.003246
TNC	2.61	0.010367
VTN	2.16	0.125593
CDH1	1.1	0.180546
NCAM1	-9.56	0.095578
TGFBI	-2.28	0.008675
TIMP2	-2.3	0.016754
VCAM1	-1.11	0.595206
RPL13A	1.26	0.945848
HPRT1	1.17	0.393554
B2M	-1.91	0.126736
GAPDH	1.47	0.09394
ACTB	1.11	0.634511

62

Figure 4: qPCR screen for cell-ECM adhesion molecules in MEP vs LEP. (A) Scatter plot showing expression of a panel of cell-ECM adhesion genes in MEP (on Y-axis) relative to LEP (on X-axis). Labeled genes showed a change in expression between LEP and MEP of at least 3-fold and a P-Value less than 0.05. **(B)** Volcano plot showing the statistical significance of each hit as a function of fold regulation. Everything above the black dotted line had a p-Value less of less than 0.05. Everything to the right or left of the dotted green and red lines had a fold change of +3 or -3. **(C)** Table summarizing fold-change and p-value in expression for a series of cell-ECM adhesion molecules of interest.

A

Expression Level in MEPs; Log(2^{-\Delta Ct(MEP)})

RPLP0
ACTB
CDH3
DSG3
DSC3
PVRL1
DLL1
DSG2
DSC2
PVRL2
PVRL4

- In RED genes overexpressed in MEPs w.r.t LEPs
- In GREEN genes underexpressed in MEPs w.r.t LEPs

Expression Level in LEPs; Log(2^{-\Delta Ct(LEP)})

B

- Log10 (P-Value)

PVRL4
DSG2
DSC2
PVRL2
TJP1
DSC3
DSG3
PVRL1
DLL1
CDH3

P-value = 0.05

RPLP0

-Log2(Fold Control of MEP/LEP)

C
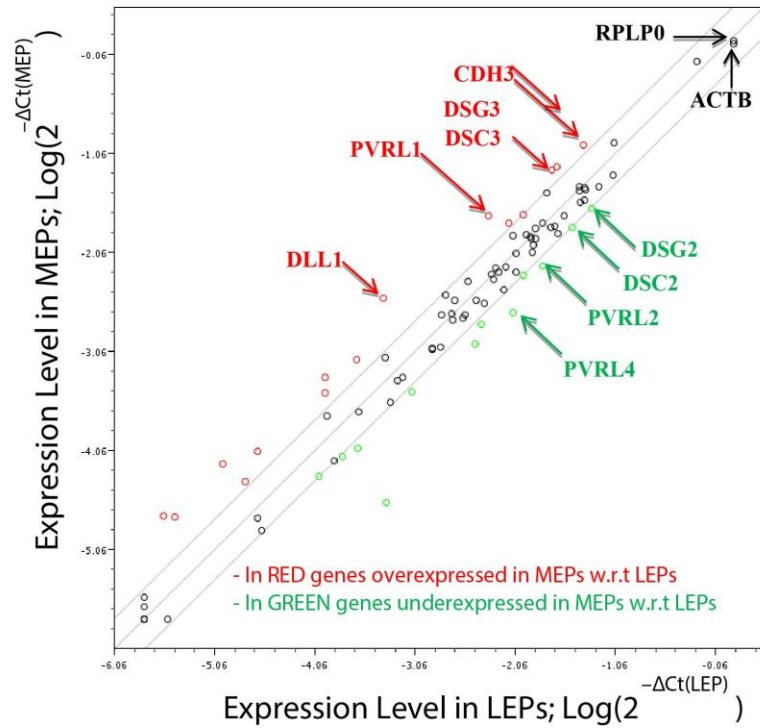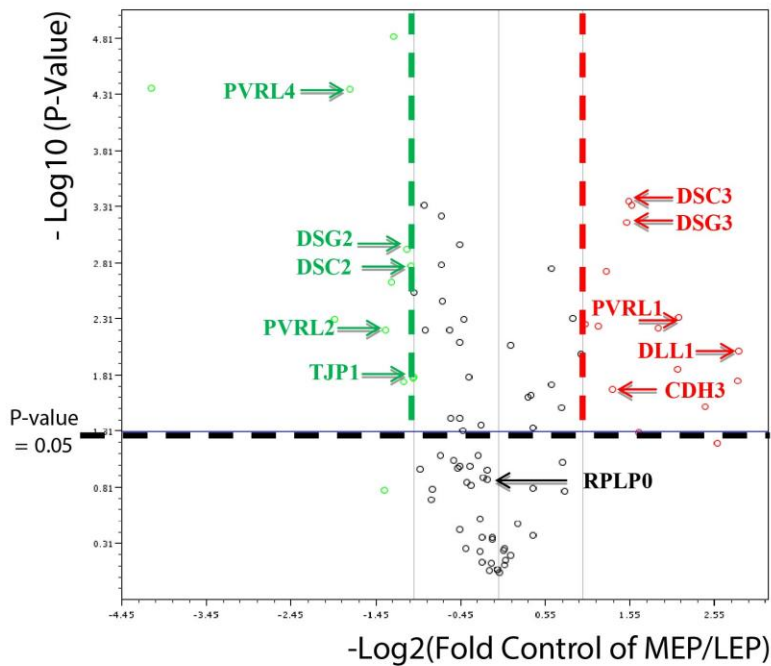
GENE	Fold Reg	P-Value
DLL1	7.1376	0.009465
CTNNA3	7.085	0.017444
P2RX6	5.4168	0.029744
PVRL1	4.3714	0.004773
PVRL3	4.3302	0.013716
DOCK4	3.7041	0.005895
DSC1	2.9617	0.000481
DSC3	2.9095	0.000445
DSG3	2.8431	0.000684
CDH3	2.537	0.020976
DSG4	2.4219	0.001867
PKP1	2.255	0.005657
FLNA	2.0187	0.00554
CDH2	-17.1788	0.000043
MAPRE2	-3.8368	0.004983
PVRL4	-3.3766	0.000044
PVRL2	-2.5301	0.006147
MLLT4	-2.4098	0.002287
BAIAP2	-2.3678	0.000015
DNM1	-2.1688	0.017836
DSG2	-2.1261	0.001182
DSC2	-2.0584	0.001646
TJP1	-2.0133	0.016625
ARVCF	-2.0049	0.016034
CDH1	-1.094	0.108166
HPRT1	-1.1428	0.718387
ACTB	-1.1855	0.080876
GAPDH	1.3017	0.023373
RPLP0	-1.098	0.132623

64

Figure 5. qPCR screen for cell-cell adhesion molecules in MEP vs LEP. (A) Scatter plot showing expression of a panel of cell-cell adhesion genes in MEP (on Y-axis) relative to LEP (on X-axis). Labeled genes showed a change in expression between LEP and MEP of at least 2-fold and a P-Value less than 0.05. **(B)** Volcano plot showing the statistical significance of each hit as a function of fold regulation. Everything above the black dotted line had a p-Value less of less than 0.05. Everything to the right or left of the dotted green and red lines had a fold change of +2 or -2. **(C)** Table summarizing fold-change and p-value in expression for a series of cell-cell adhesion molecules of interest.

4.4. Binary Cell-ECM adhesion in primary human cells directly isolated from primary tissue

Much like the fourth passage primary cells used in our previous experiments, also uncultured primary cells retained the cell-ECM binary behavior (i.e. MEPs attached and spread to surrogate ECM substrates while LEPs did not). Interestingly, the more variable and overlapping energetics of cell-cell adhesion in human primary cells that have never experienced a single passage in 2D culture was reflected by the circularity measurements shown in Figure 6. According to the DAH, this comparable work of MEP-MEP and LEP-LEP cell-cohesion explains why most of the primary tissues reconstituted in agarose self-organized into a scrambled architecture (Chapter 2, Figure 5). However, in light of the "binary" or *Digital Adhesion Hypothesis* presented in this manuscript, the use of a single interaction between the basal cells and the ECM as the governing force directing cell

sorting in adult epithelia, could explain all of the experiments presented in chapter 2 without the need to evoke the differential regulation of cell-cell cohesion.
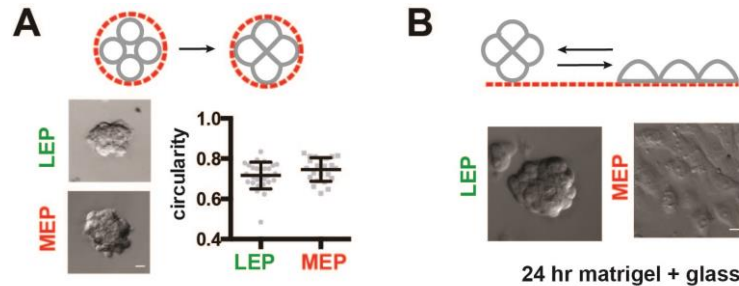
Figure 6. Cell-Cell and Cell-ECM adhesion of uncultured primary LEP and MEP at the multicellular level. (A) Circularity of pure aggregates of uncultured human primary mammary LEP and MEP cells reveals overlapping cohesive properties (n>23). **(B)** Aggregate spreading assay of pure uncultured LEP and MEP reveal the expected binary adhesive properties on Matrigel-coated surfaces.

5. Discussion

The experiments reported in this chapter suggest that in adult human tissues such as the mammary gland, the interaction between the basal (or myoepithelial) lineage and the ECM is necessary and sufficient to drive the self-organization of dissociated cells into the correct architecture. However, it was unclear weather this was due to a very high MEP-

ECM adhesion strength, a very low LEP-ECM adhesion strength, or a combination of the above. Therefore, we decided to estimate the relative work of adhesion between all cell-cell and cell-ECM pairs and to mathematically explore the biological significance of said interactions. In the next chapter we present such analysis.

Chapter 4

A mathematical model for Self-Organization in bilayered epithelia

1. Introduction

The observations presented in chapter 3 suggest that while homo- and heterotypic cell-cell cohesive interactions span a spectrum of values in the mammary gland, and are capable of directing self-organization independent of ECM into an inverted architecture, cell adhesion to the ECM boundary dominates Self-Organization and is a property unique to the MEP population. In this chapter we use our contact angle measurements in order to relate the work of cell-cell cohesion and cell-ECM adhesion in human primary mammary epithelial cells at passage 4 in culture. We conclude that $W_{MEP-ECM} > 2 x W_{MEP-MEP}$; that $W_{MEP-MEP}$, $W_{MEP-LEP}$, and $W_{LEP-LEP}$ followed the ratio of 6:3:1; and that $W_{LEP-ECM} = 0$. We use these estimates to construct a phase diagram for tissue self-assembly and to predict the self-organization of these cells under experimental perturbations to cell-cell or cell-ECM adhesion. Our computational findings support our experimental ones and reveal the strengths and limitations of a binary cell-ECM adhesion strategy.

2. Background

The goal of this analysis was to place the relative energies of different nearest neighbor interactions (e.g. cell-cell and cell-ECM) on a common scale to use as parameters in a lattice-based model of self-organization. We assume that a cell behaves as a deformable colloid with a characteristic interfacial tension that is unique to each type of interface the cell is in contact with. We ignore the microscopic and molecular causes of the interactions giving rise to these interfacial energies and treat the system as arriving at a steady state. At the steady-state, the balance of interfacial tensions (units of energy/area) of cells with other cells, surfaces, and media can be estimated using Young's equation (57). Interfacial energies can be converted to relative energies of pairwise cell-cell and cell-ECM interactions by measuring contact angles and contact areas at each interface. To simplify this analysis we assume constant surface-tension at the cell-medium interface and constant cell surface area during the duration of the assays (4 hours). We find that the work of cell-cohesion between a MEP-MEP and a LEP-MEP is approximately 6.4 and 2.8 times stronger than the work of cell-cohesion between a LEP-LEP. We also estimate that the work of ECM-adhesion between a MEP-ECM (on matrigel coated glass) is at least 4 times stronger than the work of cohesion between a MEP-MEP and that the work of adhesion between a LEP and the ECM is approximately 0. We assume that this value of MEP-ECM adhesion is an overestimate due to the high rigidity of glass relative to matrigel, which would be predicted to increase cell spreading. However, using glass in this assay significantly facilitates analysis and does not change our results. The details of our analysis follow.

2.1. Estimating the relative work of cell-cell cohesion and cell-ECM adhesion

We reason that the work of forming a cell-cell interface (W_{cc}) is the difference in energy before (E_1) and after (E_2) contact formation.
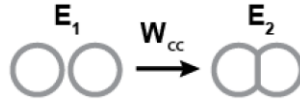
$$W_{cc} = \Delta E = E_2 - E_1 \tag{1}$$

The energy of the system before (E_1) and after (E_2) cell-cell contact can be expressed as the product of the interfacial energies and the areas of each interface:

$$E_1 = Y_{cm(1)} * A_{cm(1)}$$

$$E_2 = Y_{cm(2)} * A_{cm(2)} + Y_{cc(2)} * A_{cc(2)}$$

Where Y is the surface tension at the cell-medium (Y_{cm}) or cell-cell (Y_{cc}) interface in dimensions of energy/area, and A is the area of contact (normalized by the total surface area of a cell before and after contact) at the cell-medium (A_{cm}) or cell-cell (A_{cc}) interfaces.
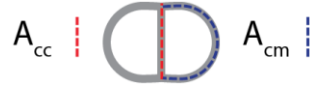
To simplify analysis, we assume that the cells have a constant surface tension at the cell-cell or cell-medium interface throughout the assay (4 hours). We also assume that the surface tension at the cell-cell interface can be expressed as a function of the surface tension at the cell-medium interface (Eq. 2) based on geometric considerations and Young's equation.
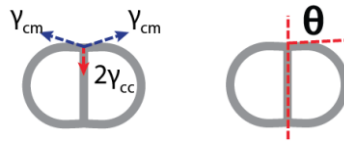
(Young)
$$Y_{cc} = Y_{cm} * \cos \theta_{cc} \tag{2}$$

Combining Eq. 1 and Eq. 2 generates a new equation (Eq. 3) that expresses the energy change (or work of cohesion) upon forming the interface between two cells.

$$W_{cc} = Y_{cm} * [A_{cm(2)} + \cos \theta_{cc} * A_{cc(2)} - A_{cm(1)}] \tag{3}$$

LEP and MEP have a similar surface tension at the cell-medium interface (i.e. $Y_{LEP-m} = Y_{MEP-m} = Y_{cm}$) based on previous measurements of the cortical elasticity of these cells by

AFM (9). We therefore relate MEP cohesion to LEP cohesion and measurable contact angles and contact areas with Eq. 4:

$$\frac{W_{MEP-MEP}}{W_{LEP-LEP}} = \tag{4}$$

$$\frac{A_{MEP-medium(2)} + \cos\theta_{MEP-MEP} * A_{MEP-MEP(2)} - A_{MEP-medium(1)}}{A_{LEP-medium(2)} + \cos\theta_{LEP-LEP} * A_{LEP-LEP(2)} - A_{LEP-medium(1)}}$$

To simplify estimating cell surface area we assume that it does not change significantly over the course of the assay and that the initial shape of the cell in the non-adhered state has the geometry of a sphere. $\theta_{MEP-MEP}$ and $\theta_{LEP-LEP}$ are determined by image analysis of cell-doublets. The average of these values is used to determine $\cos\theta_{MEP-MEP}$ and $\cos\theta_{LEP-LEP}$ and used in combination with Eq. 4 to approximate the relative energetics of MEP-MEP and LEP-LEP cohesion. A similar analysis was used to estimate the work of heterotypic MEP-LEP cohesion. Our results are summarized in Table 1.

The energy of forming a cell-ECM interface was estimated using similar reasoning: the energy released upon formation of a cell-matrix adhesion complex (W_{cx}) is the difference in energy states before (E_3) and after (E_4) complex formation (Eq. 5).
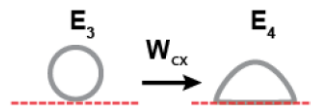
$$W_{cx} = \Delta E = E_4 - E_3 \tag{5}$$

The energy of the system before and after adhesive interface formation can be expressed as follows:

$$E_3 = Y_{cm(3)} * A_{cm(3)} + Y_{xm(3)} * A_{xm(3)}$$

$$E_4 = Y_{cm(4)} * A_{cm(4)} + Y_{cx(4)} * A_{cx(4)} + Y_{xm(4)} * A_{xm(4)}$$

Where Y is the surface tension at the cell-medium (Y_{cm}), matrix-medium (Y_{xm}), or cell-matrix (Y_{cx}) interface and A is the area of contact (normalized by the total surface area of a cell before and after contact) at the cell-medium (A_{cm}), cell-matrix (A_{cx}), or matrix-medium (A_{xm}) interface.

We similarly express the surface tension at the matrix-medium interface as a function of the surface tension at the cell-medium interface (Eq. 6) based on geometric considerations and Young's equation.

$$Y_{xm} = Y_{cx} + Y_{cm} * \cos(180° - \theta_{cx}) \tag{6}$$

73
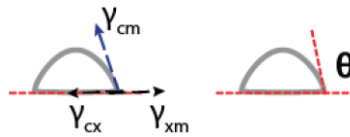
To simplify the analysis, we assume that the change in area at the matrix-medium interface is equal to the area formed at the cell-matrix interface and that cell-matrix adhesion reaches the steady state by 4 hr. Combining Eq. 5 and Eq. 6 generates a new equation (Eq. 7) that expresses the work of adhesion between a cell and the ECM.

$$W_{cx} = \Upsilon_{cm} * [A_{cm(4)} - A_{cm(3)} - A_{cx(4)} * \cos(180° - \theta_{cx})] \qquad (7)$$

Using similar reasoning as with Eq. 4 allows us to express the relative strength of a MEP-matrix adhesion with respect to a LEP-LEP adhesion as a function of measureable contact angles and contact areas.

$$\frac{W_{MEP-matrix}}{W_{LEP-LEP}} \qquad (4)$$

$$= \frac{A_{MEP-medium(4)} - A_{MEP-medium(3)} - A_{MEP-matrix(4)} * \cos(180° - \theta_{MEP-matrix})}{A_{LEP-medium(2)} + \cos \theta_{LEP-LEP} * A_{LEP-LEP(2)} - A_{LEP-medium(1)}}$$

The surface area in contact with medium was calculated by assuming the geometry of the spread cell to be that of a cone with a radius and slant height equal to the average radius and slant height of a MEP spread on the substrate as measured by confocal microscopy. The surface area in contact with ECM was calculated by measuring the perimeter of cells in contact with the substrate by analyzing Z-stack confocal images of

spread MEPs. This surface area was normalized to the average surface area of a cell modeled as a cone.

$\theta_{MEP-matrix}$ was measured by image analysis of Z-stack confocal reconstructions of cells spread on ECM-coated surfaces. The average of these values was substituted into Eq. 8 to estimate the relative strength of interaction between MEP-ECM and LEP-LEP based on the average cell-cell contact angle, cell-cell area, and cell-medium area estimated as discussed above. We note that the vast majority of LEP do not adhere to the Matrigel-coated substrate. Therefore, we estimate the work of adhesion between a LEP and the matrix to be zero ($W_{MEP-matrix} = 0$).

	$A_{cm(1)}$	$A_{cm(2)}$	$A_{cc(2)}$	$\cos(\theta_{cc})$	$W_{cc}/W_{LEP\text{-}LEP}$
MEP-MEP	1.000	0.795	0.205	0.358	6.417
MEP-LEP	1.000	0.857	0.143	0.602	2.775
LEP-LEP	1.000	0.930	0.070	0.707	1.000

	$A_{cm(3)}$	$A_{cm(4)}$	$A_{cx(4)}$	$\cos(180-\theta_{cx})$	$W_{cx}/W_{LEP\text{-}LEP}$
MEP-X	1.000	0.532	0.468	0.193	27.222
LEP-X	N/A	N/A	N/A	N/A	0.000

Table 1. Summary of estimated normalized interfacial areas and relative works of cell-cell cohesion and cell-ECM adhesion normalized to the work of cohesion between LEP-LEP.

To test the impact of our assumptions on the relative values of cell-cell cohesion and cell-ECM adhesion, we re-evaluated the values reported in Table 1 based on different assumptions. For instance, if we estimate the total area of a cell before spreading as the area of a sphere but the total area of the cell after spreading as the area of a cone, the cell surface area is increased by approximately 27 %. Although this would imply that the work of adhesion between a MEP and the matrix is 21 (and not 27) times stronger than the work of cohesion between two LEPs, the MEP-matrix interaction is still at least 3 times stronger than the work of cohesion between 2 MEPs. However, as we will see later, the tissue boundary can dominate self-organization even when it is considerably weaker than cell-cell adhesion. Therefore, these values are still strikingly higher than what would be

necessary to drive robust self-organization. Finally, it is important to mention that for our computational experiments we estimate the work of adhesion between a MEP and the ECM to be only 16 times stronger than the work of adhesion between two LEPs because this was the most conservative value we could estimate after challenging each assumption in our analysis (see reference 5 for details).

3. Methods

3.1. Computational Model

Using the estimated works of cell-cell and cell-ECM adhesion described above, we formulated a simple but general lattice model of cell sorting inspired by the models of Steinberg and Glazier (2, 58). These classic models analyze self-organization of a tissue through cell sorting as an energy minimization problem analogous to known problems in statistical mechanisms where an equilibrium macroscopic ordering of a system is achieved through local interactions between particles. The fundamental assumption in statistical mechanics inspired models of cell sorting is that the dynamics of cells within a tissue bring the system to a kind of equilibrium state that maximizes the total cellular cohesion by minimizing an effective internal energy. Several different flavors of lattice cell sorting models have been proposed. However, for this work we used a computationally efficient model that enabled complete reconstruction of the DAH phase diagrams previously

discussed, analysis of how variability in interaction energies between cells impacts self-organization, and analytic calculations. The details of how this model was constructed and used can be found in the supplementary information of reference 5.

3.2. Protein knockdown and perturbations to Cell-Cell and Cell-ECM adhesion

Conditions for transfection of HMEC with siRNA were optimized using cells grown in 12 well plates and with siRNA targeting cell surface adhesion molecules α_6 or β_1 integrin (Fig. 1). Cells grown in 10 cm dishes were transfected with Smartpool siRNA (Dharmacon/Thermo) targeting Talin1, p120 catenin, or a non-silencing control (NSC) 72 hours prior to sorting (i.e. maximum knock-down). Transfections were performed with 75 nM siRNA using Dharmafect 2 transfection reagent following the manufacturer's protocol. Successful knock down of target proteins was confirmed by western blot and/or flow cytometery as shown in Figure 1. Physical consequences of knockdown were quantified using contact angle and circularity assays (Fig. 3). It is important to note that for measuring Cell-ECM contact angle assay, we visually screened for cells that did not exhibit extensive membrane damage that occurred in occasional cells after delivery of siRNA reagents.
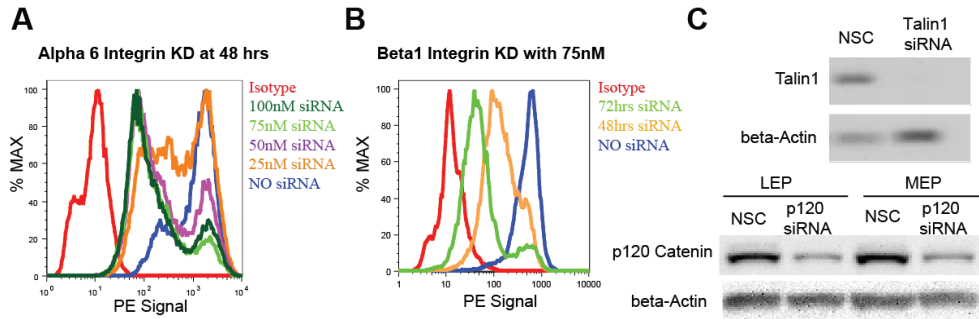
Figure 1: *Optimization, verification, and characterization of siRNA experiments.* **(A)** Flow cytometry analysis of optimal siRNA concentration using the knockdown of α_6 integrin as a model target. **(B)** Flow cytometry analysis of optimal transfection time for the knockdown of β_1 integrin as a model target. **(C)** Western blot of HMEC transfected with siRNA targeting Talin1. **(D)** Western blot of HMEC transfected with siRNA targeting p120-catenin. After transfection, HMEC were sorted into LEP and MEP to confirm knock down in both lineages.

4. Results

4.1. The MEP-ECM adhesion need not be the strongest interaction to dominate self-organization.

In contrast to individual cell-cell interactions, cell-ECM interactions are spatially restricted to the outer edge of the tissue where basement membrane components accumulate. This qualitative difference between cell-cell and cell-ECM interactions could have important consequences on the robustness of self-organization, but the relative contribution of these spatial constraints is unclear. We therefore implemented a coarse-

grained and lattice-based mathematical model that compares the relative stability of the correct and inverted architectures as a function of tissue geometry and the relative stability of each type of cell-cell and cell-ECM interaction (Fig. 2). In this model, we treated ECM as a set of static cells that define the tissue boundary. We calculated that a phase transition between the inverted and correct tissue architectures would occur when $W_{MEP\text{-}ECM}$ satisfies the following inequality:

$$W_{MEP-ECM} > (W_{MEP-MEP} - W_{LEP-LEP}) * \emptyset(r) + W_{LEP-ECM}$$

where $\emptyset(r)$ is a geometric parameter (5). For the measured relative energies of cell-cell interactions discussed above and the given model geometry of the human mammary tissue, the correct tissue architecture is the most stable for values of $W_{MEP-ECM} > 2.5 * W_{LEP-LEP}$. Surprisingly, this value of $W_{MEP\text{-}ECM}$ is less than the magnitude of both $W_{MEP\text{-}MEP}$ and $W_{MEP\text{-}LEP}$ in the model. Therefore, this inequality highlights the importance of a spatially restricted adhesive cue on self-organization. It also highlights the importance of an all-or-nothing (i.e. binary) adhesive interaction between each cell type and the tissue-ECM boundary (i.e. $W_{LEP-ECM} = 0$), because the strength of $W_{MEP-ECM}$ necessary to correct an inverted architecture increases directly with the strength of $W_{LEP-ECM}$. If the energy of LEP-ECM adhesion is maintained near zero, MEP-ECM adhesion can dominate tissue self-organization even when it is weaker than individual cell-cell interactions.

4.2. An adhesive tissue boundary sustains self-organization upon perturbation to cell-cell cohesion

To explore the robustness of self-organization to varied parameters mimicking plasticity in the strength of interactions among and between each cell type, we implemented the mathematical model computationally. We first confirmed that the computational model converged on the correct and inverted tissue architecture in the presence or absence of an adhesive ECM, respectively (Fig. 2, 5). We then tested combinations of parameters for cell-cell interactions across 10,000 runs of the model, and plotted the results of each run as a sphere on a 3D phase diagram. Each sphere's color corresponds to distinct tissue configurations (Fig. 2C). In the presence of an adhesive ECM boundary, we found that the correct configuration (red sphere) was stable across the majority of sampled parameters. In contrast, tissue configuration was exquisitely sensitive to changes to the hierarchy of cell-cell interactions in the absence of an adhesive tissue boundary. Indeed, the tissue seemed poised near numerous phase boundaries such that small perturbations to parameters triggered large-scale transitions between dissimilar tissue architectures.
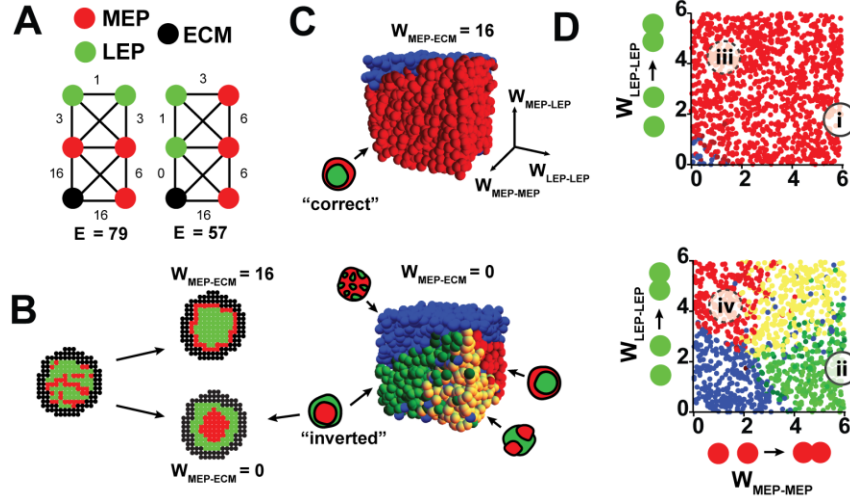
Figure 2: A lattice-based model of self-organization predicts a striking robustness to perturbations of cell-cell cohesion in the presence of an adhesive tissue boundary. (A) Two configurations of LEP (green), MEP (red), and ECM (black) with different net energies. Numbers on edges represent the energies (relative to LEP-LEP) of specific interactions derived from contact angle measurements. **(B)** The outcome of Monte-Carlo simulations using the indicated values for $W_{MEP-ECM}$ for tissue self-organization on a square lattice with stationary ECM cells. **(C)** Phase diagrams for tissue self-organization in the presence (top) and absence (bottom) of MEP-ECM interactions. Each sphere represents a single run of the model. Color represents the indicated tissue architecture (small icons). Increasing the MEP-ECM interaction moves the phase boundary at the top of the diagram in the vertical direction. **(D)** Cross sections through the phase diagrams in C reveal the combinations of parameters representative of fourth passage primary mammary epithelial cells (i). Positions (ii)-(iv) represent sets of parameters resulting from different types of perturbations.

More detailed visual analysis of the phase diagram suggested several testable hypotheses (Fig. 2D). First, tissue self-organization should be robust to pronounced decreases of MEP-MEP or LEP-LEP cohesion in the presence of an adhesive ECM boundary (e.g. perturbation i → iii). In contrast, the same perturbations should lead to a

transition between dissimilar tissue configurations in the absence of an adhesive ECM boundary (e.g. perturbation ii → iv).

4.3. Impaired cell-cell cohesion doe*s not prevents proper self-organization in Matrigel*

To measure the impact of perturbations to cell-cell cohesion on self-organization, we used siRNA to knock down critical cell-cell or cell-ECM adaptor molecules that significantly contribute to cell-cell or cell-ECM adhesion. As shown in Figure 3, p120 catenin is necessary for stabilizing cadherin mediated cell-cell interfaces. Therefore, knock down of p120 catenin caused a dramatic reduction in MEP-MEP cohesion as determined by a decrease in contact angle and a reduction in aggregate circularity. However, p120 knock down did not have a significant effect on cell-ECM contact angle over a similar timeframe. To assay for self-organization, we forced aggregation of control LEP with p120 knock-down MEP by either mechanical or chemical means. Consistent with the predictions of the model, we observed a transition among tissue architectures in agarose: instead of an inverted tissue architecture, the now less cohesive MEPs moved to the periphery of the tissue, allowing the now more cohesive control LEPs to maximize their interactions at the tissue core (Fig. 3D). However, the decrease in MEP-MEP cohesion did not alter the outcome of self-organization in Matrigel, where control LEP remained in the tissue core and p120 knock-down MEP adhered to the boundary (Fig. 3, E and F).
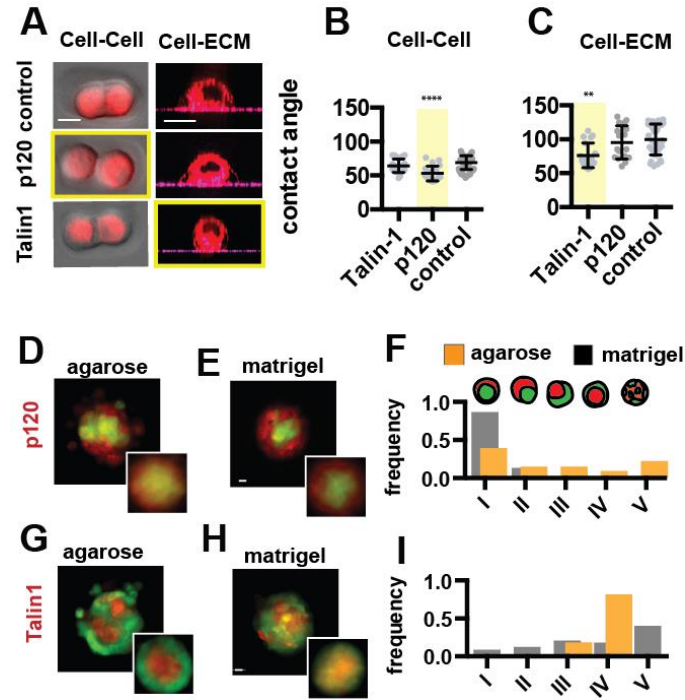
Figure 3: Self-organization is robust to perturbation of cell-cell cohesion only in the presence of an adhesive tissue boundary. (**A**) Representative images used to measure contact angles at the cell-cell and cell-ECM interfaces for the given perturbations. (**B**) Contact angles (and SD) at the cell-cell and (**C**) cell-ECM interfaces upon the indicated perturbation (control = non-silencing control; n = 16-56). Measurements for Talin-1 knock-down cells do not account for a significant fraction of the population which do not adhere to matrix and are removed during wash steps. (**D**) Representative image and average intensity plots (inset, n=20) for p120 knock-down MEP self-organized with control LEP in agarose and (**E**) Matrigel. (**F**) Distributions of tissue architectures from D and E indicate a shift from configuration IV towards configuration I in agarose, but no change in tissue configuration in Matrigel (n=45-54). (**G**) Representative image and average intensity profiles (inset, n=20) for Talin-1 knock-down MEP with control LEP in agarose and (**H**) Matrigel. (**I**) Distributions of tissue architectures from G and H indicate a shift from the correct to inverted architecture in Matrigel upon Talin-1 knock down, but no change in agarose (n=72-81).

4.4. Impaired MEP-ECM adhesion prevents proper self-organization in Matrigel

The computational model also predicts that a loss of matrix adhesion in the MEP population should be sufficient to trigger a transition to the inverted architecture, independent of the physical or chemical properties of the surrounding matrix. Thus, interfering with adhesion between MEP and Matrigel should trigger a transition in tissue architecture similar to that seen in agarose. We therefore targeted the protein Talin-1 for knock down. Talin-1 is a critical adapter protein necessary for linking the actomyosin cytoskeleton to integrins. Therefore, loss of Talin-1 prevents cells from mechanically coupling their contractile apparatus to the ECM. Knock-down of Talin-1 caused a reduction in MEP adhesion measured by a decrease in contact angle at the MEP-ECM interface (Fig. 3, A and C). However, Talin-1 knock-down did not have an effect on cell-cell contact angle measurements at four hours (Fig. 3B), although we did observe a reduction in MEP aggregate circularity at the multicellular level that is consistent with previous reports that highlight the role of integrins in mediating cell-cell adhesion (59). These Talin-1 knockdown cells assembled efficiently into the inverted architecture with control LEP in agarose, as would be expected for populations of cells with near wild-type cell-cell contact angles (Fig. 3G). In Matrigel, however, Talin-1 knockdown cells no longer formed the correct architecture efficiently with control LEP – consistent with their reduced MEP-ECM contact angle. Instead, we observed a significant enrichment for the inverted architecture (Fig. 3, H and I).

Taken together, these experiments indicate that MEP-ECM adhesion is necessary and sufficient for correct cell positioning. Moreover, this dominant and binary adhesive interaction renders mammary gland self-organization robust to perturbation to the hierarchy of cell-cell interactions among luminal and myoepithelial cells, as p120 knockdown does not affect cell positioning despite having a profound affect on cell-cell cohesion.

4.5. Computational Validation

Finally, we revised the computational model to test the extent to which a binary adhesive interaction with the tissue boundary renders self-organization robust to cell-to-cell variability. In the revised model, energies of interaction for individual cells of a given cell-type were drawn from a distribution of values rather than from a single value as in previous cases (Fig. 4A, 5). The model produced qualitatively similar observations to those seen in Matrigel and agarose as the variability in each population approached the average difference in their cell-cell cohesion energies: increased variability had little impact on the correct architecture in the presence of an adhesive ECM boundary, while the inverted architecture trended towards disorganization in the absence of an adhesive ECM boundary (Fig. 4B and 4C). Along with our experimental results, this model suggests that a dominant and binary adhesive interaction between one cell type and the tissue-ECM boundary imparts considerable robustness to the self-organization.

Figure 4: A "digital" or "binary" adhesion to the ECM boundary supports self-organization among variable and heterogeneous populations of cells. (A) Distribution of homotypic interaction energies drawn from a log-normal distributions and having a $\sigma/d\mu = 1.5$. **(B)** Simulated self-organization of human mammary epithelial cells in agarose (left) and Matrigel (right), but with $\sigma/d\mu = 1.5$. **(C)** The relative efficiency of self-organization to an identical tissue architecture (configuration I) as a function of cell-to-cell variability using a strategy of strong and binary ECM adhesion (black; $W_{MEP\text{-}ECM} = 2xW_{MEP\text{-}MEP}$) or differential cell-cell interactions alone (red).

5. Discussion

A balance between multiple cellular interactions is believed to direct self-organization in a variety of contexts. During development, changes to this balance of interaction can be used to drive tissue rearrangements and morphogenesis (60). In adult tissues, however, disrupting this balance of interactions would disrupt the capacity of tissues to retain a single correct architecture. Such conditions can occur in heterogeneous cell populations or when cellular properties are plastic in order to adapt to the changing needs of a dynamic tissue. Using primary human mammary epithelial cells as a model

system, we confirm this notion and show that self-organization through a hierarchy of cell-cell cohesive interactions is sensitive to perturbation and cell-to-cell variability. To provide robustness to this process, we find that the outer myoepithelial population adheres to basement membrane components it deposits at the tissue boundary. This adhesive interaction is the dominant interaction among mammary epithelial cells. Surprisingly, this interaction is also binary, in that it is unique to the MEP cells. Modeling studies suggest that adhesion of MEP to the tissue boundary can supersede stronger cell-cell cohesive interactions, so long as LEP adhesion to the tissue boundary is maintained near zero. Thus, this dominant, self-generated, and binary adhesive interaction drives the rapid collapse of the MEP population to the tissue edge. Control of self-organization by the properties of the surrounding medium is conceptually analogous to protein folding, where hydrophobic collapse is dominated by the energetics of hydrophobic and hydrophilic amino acid side-chain interactions with the aqueous solvent (61).

6. Conclusion

The finding that cell-cell cohesion is dispensable in guiding cell positioning is surprising, but consistent with genetic data from mouse models. For example, ablation of P- or E-cadherin during mouse mammary gland development does not dramatically alter basic tissue architecture (62-64). Furthermore, also ablation of p120 catenin during mammary gland development did not change the relative positioning of MEP and LEP with respect to the tissue boundary, although it did trigger glandular thickening and lumen filling (65). On its surface, our finding that MEP-ECM adhesion dominates tissue self-organization seems inconsistent with numerous reports that also integrins are dispensable during mouse mammary gland development. However, it is important to mention that MEP express numerous integrins that appear to be able to partially compensate for one another in the process of self-organization. Indeed, in our cell-sorting experiments, knock down of key integrins such as B1 or A6 in MEP did not alter tissue self-organization (not shown) and only perturbations affecting all members of the integrin family effected both MEP-ECM contact angle measurements and self-organization. This is consistent with mouse data, where ablation of proteins that interact with multiple integrins such as FAK, have a pronounced phenotype on mammary tissue architecture, triggering a breakdown of the MEP and LEP epithelial compartments and a mixing of the two cell populations (66).

The dominant role of myoepithelial cells in guiding the self-organization of the mammary gland is particularly interesting considering their purported role as cellular tumor suppressors and master regulators of tissue architecture (56). Moreover, the critical role of

MEP-ECM interactions in driving tissue self-organization is also consistent with a role for matrix composition and mechanical properties in guiding the outcome of morphogenesis, tumor progression and cancer cell dissemination (67, 68). Indeed, our results would indicate that regulating the balance of MEP-ECM adhesion or MEP-MEP cohesion could play a significant role in driving changes to tissue architecture during morphogenesis (69). More interestingly, our results suggest that increases in LEP-ECM adhesion could have even more profound changes on tissue architecture, such as those that occur during distinct stages of malignant disease (69-71). However, future efforts will be needed to dissect the precise relationship between matrix mechanical properties, cell-cell cohesive properties, tissue geometry, and the capacity of LEP and MEP to form, retain, and remodel the correct architecture of the mammary gland.

7. Final remarks

Why assemble a tissue using a binary and self-generated adhesive interaction at the tissue-ECM boundary, rather than through a balance of cell-cell interactions? Guiding structure formation through a balance of cell-cell interactions alone is exquisitely sensitive to changes in the strength of individual cell-cell interactions. Therefore, this strategy is useful for driving transitions between tissue architectures in developmental contexts, but would lead to a breakdown in architecture in adult tissues when cell properties change (30). In contrast, the influence of an adhesive tissue boundary on self-organization dominates

cell-cell cohesive interactions of similar magnitude. Therefore, to sustain the basic architecture of the mammary gland in the context of dynamic processes like morphogenesis, it is sufficient to simply maintain one cell-ECM interaction near zero (i.e. the LEP).

While one could also imagine a robust strategy of tissue self-organization using very large differences in the strength of cell-cell interactions, assembling a tissue using such parameters would have important consequences on the kinetics of tissue formation, as large barriers would exists to exchanging cell positions for the most cohesive cell type, and consequently, this component of the tissue would behave more like a glass than a liquid (72).

So what, if any, costs are associated with assembling a tissue using a dominant interaction between one cell type and the tissue-ECM boundary? Because of the reliance of this strategy on the surface area of the tissue, it will fail as the surface to volume ratio of a tissue grows beyond a certain critical threshold (5). This fact is captured in the scaling parameter ($\emptyset(r)$) we included in the mathematical model. Thus, this mechanism of tissue formation, maintenance, and repair seems uniquely suited to the many tissues that consist of small aggregates or tubes comprising two cell types that must maintain a stereotyped organization relative to each other and the surrounding ECM.

References

1. Lancaster MA, Knoblich JA (2014) Organogenesis in a dish: Modeling development and disease using organoid technologies. Science 345:283-286.

2. Steinberg MS (1963) Reconstruction of tissues by dissociated cells. Some morphogenetic tissue movements and the sorting out of embryonic cells may have a common explanation. *Science* 141:401–408.

3. Townes PL, Holtfreter J (1955) Directed Movements and Selective Adhesion of Embryonic Amphibian Cells. *J Exp Zool* 128:53–120.

4. Cerchiari et al. (2014) Formation of spatially and geometrically controlled 3D tissues in soft gels via Sacrificial Micromolding. In Review.

5. Cerchiari et al. (2014) A strategy for tissue Self-Organization that is robust to cellular heterogeneity and plasticity. In Review.

6. Pampaloni F, Reynaud EG, Stelzer EHK (2007) The third dimension bridges the gap between cell culture and live tissue. *Nat. Rev. Mol. Cell Biol.* 8:839–45.

7. Griffith LG, Swartz MA, (2006) Capturing complex 3D tissue physiology in vitro. *Nat. Rev. Mol. Cell Biol.* 7:211–24.

8. Kane RS, Takayama S, Ostuni E, Ingber DE, Whitesides GM (1999) Patterning proteins and cells using soft lithography. *Biomaterials* 20:2363–76.

9. Chanson L et al. (2011) Self-organization is a dynamic and lineage-intrinsic property of mammary epithelial cells. *Proc. Natl. Acad. Sci. U. S. A.* 108:3264–3269.

10. Guo C, Ouyang M et al. (2012) Long-range mechanical force enables self-assembly of epithelial tubular patterns. *Proc. Natl. Acad. Sci. U. S. A.* 109:5576-82.

11. Karp JM *et al.* (2007) Controlling size, shape and homogeneity of embryoid bodies using poly(ethylene glycol) microwells. *Lab Chip* 7:786–94.

12. Nelson CM. *et al.* (2005) Emergent patterns of growth controlled by multicellular form and mechanics. *Proc. Natl. Acad. Sci. U. S. A.* 102:11594–9.

13. Hughes CS, Postovit LM, Lajoie GA (2010) Matrigel: a complex protein mixture required for optimal growth of cell culture. *Proteomics* 10:1886–90.

14. Kleinman HK *et al.* (1986) Basement membrane complexes with biological activity. *Biochemistry* 25:312–318.

15. Soofi SS, Last, JA, Liliensiek SJ, Nealey PF, Murphy CJ (2009) The elastic modulus of Matrigel as determined by atomic force microscopy. *J. Struct. Biol.* 167:216–9.

16. Sodunke TR *et al.* (2007) Micropatterns of Matrigel for three-dimensional epithelial cultures. *Biomaterials* 28:4006–16.

17. Baker BM, Trappmann B, Stapleton SC, Toro E, Chen CS (2013) Microfluidics embedded within extracellular matrix to define vascular architectures and pattern diffusive gradients. *Lab Chip* 13:3246–52.

18. Golden AP, Tien J (2007) Fabrication of microfluidic hydrogels using molded gelatin as a sacrificial element. *Lab Chip* 7:720–5.

19. Liu JS, Farlow JT, Paulson AK, Labarge, MA, Gartner ZJ (2012) Programmed cell-to-cell variability in Ras activity triggers emergent behaviors during mammary epithelial morphogenesis. *Cell Rep.* 2:1461–70.

20. Kam KR. *et al.* (2013) Nanostructure-mediated transport of biologics across epithelial tissue: enhancing permeability via nanotopography. *Nano Lett.* 13:164–71.

21. Tang MD, Golden AP, Tien J (2003) Molding of three-dimensional microstructures of gels. *J. Am. Chem. Soc.* 125:12988–9.

22. Debnath J, Muthuswamy SK, Brugge JS (2003) Morphogenesis and oncogenesis of MCF-10A mammary epithelial acini grown in three-dimensional basement membrane cultures. *Methods* 30:256–268.

23. Ivanov AI *et al. (2008)* Myosin II regulates the shape of three-dimensional intestinal epithelial cysts. *J. Cell Sci.* 121:1803–14.

24. Martín-Belmonte F *et al.* (2008) Cell-polarity dynamics controls the mechanism of lumen formation in epithelial morphogenesis. *Curr. Biol.* 18:507–13.

25. Datta A, Bryant DM, Mostov KE (2011) Molecular regulation of lumen morphogenesis. *Curr. Biol.* 21:R126–36.

26. Beck JN, Singh A, Rothenberg AR, Elisseeff JH, Ewald AJ (2013) The independent roles of mechanical, structural and adhesion characteristics of 3D hydrogels on the regulation of cancer invasion and dissemination. *Biomaterials* 34:9486–95.

27. Nguyen-Ngoc K-V, Ewald AJ (2013) Mammary ductal elongation and myoepithelial migration are regulated by the composition of the extracellular matrix. *J. Microsc.* 251:212–23.

28. Sasai Y (2013) Cytosystems dynamics in self-organization of tissue architecture. *Nature* 493:318–326.

29. Xiong F et al. (2013) Specified Neural Progenitors Sort to Form Sharp Domains after Noisy Shh Signaling. *Cell* 153:550–561.

30. Dietrich J-E, Hiiragi T (2007) Stochastic patterning in the mouse pre-implantation embryo. *Development* 134:4219–4231.

31. Runswick SK, O'hare MJ, Jones L, Streuli CH, Garrod DR (2001) Desmosomal adhesion regulates epithelial morphogenesis and cell positioning. *Nat Cell Biol* 3:823–830.

32. Rudland PS (1991) Histochemical organization and cellular composition of ductal buds in developing human breast: evidence of cytochemical intermediates between epithelial and myoepithelial cells. *J Histochem Cytochem* 39:1471–1484.

33. Gudjonsson T, Adriance MC, Sternlicht MD, Petersen OW, Bissell MJ (2006) Myoepithelial Cells: Their Origin and Function in Breast Morphogenesis and Neoplasia. *J Mammary Gland Biol Neoplasia* 10:261–272.

34. Ewald AJ, Brenot A, Duong M, Chan BS, Werb Z (2008) Collective epithelial migration and cell rearrangements drive mammary branching morphogenesis. *Dev Cell* 14:570–581.

35. Mailleux AA et al. (2007) BIM Regulates Apoptosis during Mammary Ductal Morphogenesis, and Its Absence Reveals Alternative Cell Death Mechanisms. *Developmental Cell* 12:221–234.

36. Gjorevski N, Nelson CM (2011) Integrated morphodynamic signaling of the mammary gland. Nat. Rev. Mol. Cell Bio. 12:581-593.

37. Altschuler SJ, Wu LF (2010) Cellular heterogeneity: do differences make a difference? *Cell* 141:559–563.

38. Chang HH, Hemberg M, Barahona M, Ingber DE, Huang S (2008) Transcriptome-wide noise controls lineage choice in mammalian progenitor cells. *Nature* 453:544–547.

39. Eldar A, Elowitz MB (2010) Functional roles for noise in genetic circuits. *Nature* 467:167–173.

40. Khan SA, Rogers MA, Khurana KK, Meguid MM, Numann PJ (1998) Estrogen receptor expression in benign breast epithelium and breast cancer risk. *J Natl Cancer Inst* 90:37–42.

41. Moreira JMAJ et al. (2010) Tissue proteomics of the human mammary gland: Towards an abridged definition of the molecular phenotypes underlying epithelial normalcy. *Mol Oncol* 4:23–23.

42. Keller PJ et al. (2010) Mapping the cellular and molecular heterogeneity of normal and malignant breast tissues and cultured cell lines. *Breast Cancer Research* 12:R87.

43. Shehata M et al. (2012) Phenotypic and functional characterization of the luminal cell hierarchy of the mammary gland. *Breast Cancer Res* 14:R134.

44. Bloushtain-Qimron N et al. (2008) Cell type-specific DNA methylation patterns in the human breast. *Proc Natl Acad Sci USA* 105:14076–14081.

45. Santagata S et al. (2014) Taxonomy of breast cancer based on normal cell phenotype predicts outcome. *The Journal of Clinical Investigation* 124:859–870.

46. Stampfer MR, LaBarge MA, Garbe JC (2013). An Integrated Human Mammary Epithelial Cell Culture System for Studying Carcinogenesis and Aging. *Cell and Molecular Biology of Breast Cancer*, (Chapter 15): 323–361.

47. Zhao H, Nolley R, Chen Z, Peehl DM (2010) Tissue slice grafts: an in vivo model of human prostate androgen signaling. *The American Journal of Pathology*, *177*(1):229–239.

48. Peehl DM (2002) Human prostatic epithelial cells (Second Edition). New York: Culture of epithelial cells.

49. Liu JS, Farlow JT, Paulson AK, LaBarge MA, Gartner ZJ (2012) Programmed Cell-to-Cell Variability in Ras Activity Triggers Emergent Behaviors during Mammary Epithelial Morphogenesis. *Cell Reports* 2:1461–1470.

50. Selden, N. S., Todhunter, M. E., Jee, N. Y., Liu, J. S., Broaders, K. E., & Gartner, Z. J. (2012). Chemically programmed cell adhesion with membrane-anchored oligonucleotides. *Journal of the American Chemical Society*, *134*(2), 765–768.

51. Gartner ZJ, Bertozzi CR (2009) Programmed assembly of 3-dimensional microtissues with defined cellular connectivity. *Proc. Nat. Acad. Sci. U. S. A.106*: 4606–4610.

52. Todhunter M, Jee N et al. (2014) Rapid Synthesis of 3D Tissues by Chemicallly Programmed Assembly. In Review.

53. Garbe JC et al. (2012) Accumulation of multipotent progenitors with a basal differentiation bias during aging of human mammary epithelia. *Cancer Res* 72:3687–3701.

54. Foty RA, Steinberg MS (2005) The differential adhesion hypothesis: a direct evaluation. Dev. Biol. 278:255-63.

55. Lim CT et al. (2006) Mechanical models for living cells - a review. Journal of Biomechanics 39:195-216.

56. Adriance MC, Inman JL, Petersen OW, Bissell MJ (2005) Myoepithelial cells: good fences make good neighbors. *Breast Cancer Res* 7:190–197.

57. Maître J-L et al. (2012) Adhesion Functions in Cell Sorting by Mechanically Coupling the Cortices of Adhering Cells. *Science* 338:253–256.

58. Glazier JA, Graner F (1993) Simulation of the differential adhesion driven rearrangement of biological cells. Phy. Rev. E 47:2128-54.

59. Robinson EE, Zazzali KM, Corbett SA, Foty RA (2003) Alpha5beta1 integrin mediates strong tissue cohesion. *J Cell Sci* 116:377–386.

60. Ohnishi Y et al. (2013) Cell-to-cell expression variability followed by signal reinforcement progressively segregates early mouse lineages. *Nat Cell Biol*.

61. Dill KA et al. (1995) Principles of protein folding--a perspective from simple exact models. *Protein Sci* 4:561–602.

62. Radice GL et al. (1997) Precocious mammary gland development in P-cadherin-deficient mice. *J Cell Biol* 139:1025–1032.

63. Evers B et al. (2010) A tissue reconstitution model to study cancer cell-intrinsic and -extrinsic factors in mammary tumourigenesis. *J Pathol* 220:34–44.

64. Boussadia O, Kutsch S, Hierholzer A, Delmas V, Kemler R (2002) E-cadherin is a survival factor for the lactating mouse mammary gland. *Mechanisms of Development* 115:53–62.

65. Kurley SJ et al. (2012) p120-catenin is essential for terminal end bud function and mammary morphogenesis. *Development* 139:1754–1764.

66. Van Miltenburg MHAM et al. (2009) Complete focal adhesion kinase deficiency in the mammary gland causes ductal dilation and aberrant branching morphogenesis through defects in Rho kinase-dependent cell contractility. *FASEB J* 23:3482–3493.

67. Beck JN, Singh A, Rothenberg AR, Elisseeff JH, Ewald AJ (2013) The independent roles of mechanical, structural and adhesion characteristics of 3D hydrogels on the regulation of cancer invasion and dissemination. *Biomaterials* 34:9486–9495.

68. Butcher DT, Alliston T, Weaver VM (2009) A tense situation: forcing tumour progression. *Nat Rev Cancer* 9:108–122.

69. Basham KJ et al. (2013) Chemical Genetic Screen Reveals a Role for Desmosomal Adhesion in Mammary Branching Morphogenesis. *Journal of Biological Chemistry* 288:2261–2270.

70. Nguyen-Ngoc K-V et al. (2012) ECM microenvironment regulates collective migration and local dissemination in normal and malignant mammary epithelium. *Proc Natl Acad Sci USA* 109:E2595–E2604.

71. Cheung KJ, Gabrielson E, Werb Z, Ewald AJ (2013) Collective Invasion in Breast Cancer Requires a Conserved Basal Epithelial Program. *Cell*.
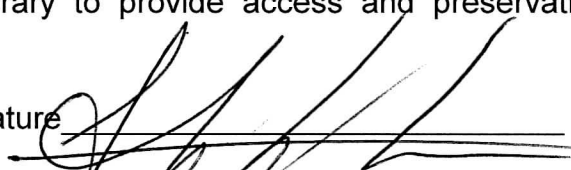
72. Schötz E-M, Lanio M, Talbot JA, Manning ML (2013) Glassy dynamics in three-dimensional embryonic tissues. *J R Soc Interface* 10:20130726–20130726.

Publishing Agreement

It is the policy of the University to encourage the distribution of all theses, dissertations, and manuscripts. Copies of all UCSF theses, dissertations, and manuscripts will be routed to the library via the Graduate Division. The library will make all theses, dissertations, and manuscripts accessible to the public and will preserve these to the best of their abilities, in perpetuity.

I hereby grant permission to the Graduate Division of the University of California, San Francisco to release copies of my thesis, dissertation, or manuscript to the Campus Library to provide access and preservation, in whole or in part, in perpetuity.

Author Signature _____ Date _Sept. 15TH, 2014_

(This final page must be signed and dated and should be numbered.)